Volume 3, Number 1 March 2021

# Nanomaterials Science & Engineering

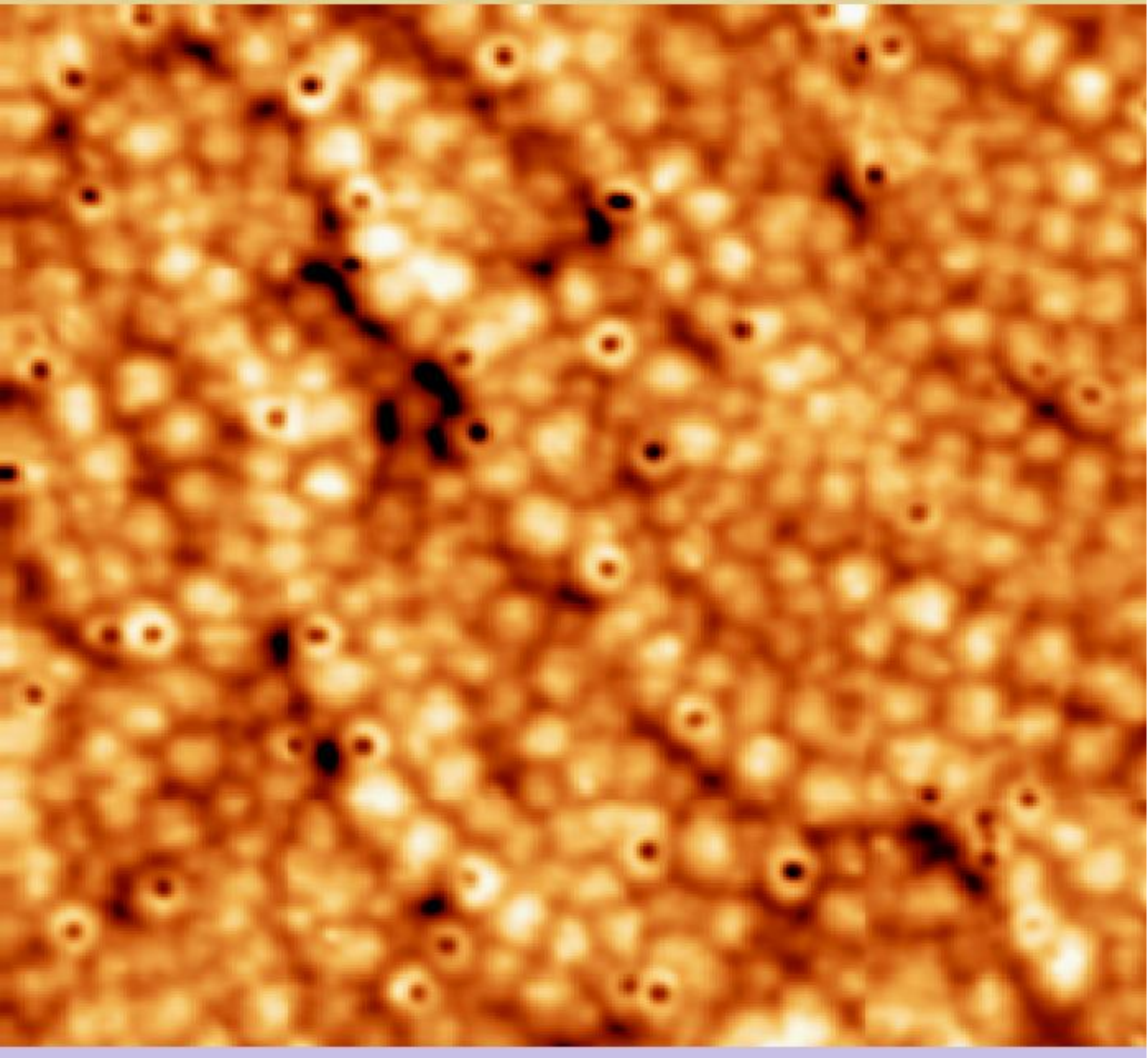

university of aveiro tema centre for mechanical technology and automation

*Volume 3, Number 1* *December 2021*

# Nanomaterials Science & Engineering

university of aveiro tema centre for mechanical technology and automation

**Title**
Nanomaterials Science & Engineering (NMS&E), Vol.3, No.1, 2021

**Editors-in-Chief**
Igor Bdikin
Paula Alexandrina de Aguiar Pereira Marques
Duncan Paul Fagg

**Editorial Managers**
Igor Bdikin
Gil Gonçalves
Raul Simões

**Cover and Logo**
Igor Bdikin, Sérgio Manuel de Sousa Pereira (InGaN/GaN quantum dots heterostructure, AFM image, 2x2x0.002 $\mu m^3$)

**Publisher**
University of Aveiro

**Support**
Serviços de Biblioteca, Informação Documental e Museologia
Centre for Mechanical Technology & Automation (TEMA)
Mechanical Engineering Department
University of Aveiro

**Mailing Address**
Department of Mechanical Engineering
University of Aveiro
Aveiro 3810-193
Portugal
E-mail: bdikin@ua.pt

**ISSN:** 2184-7002

## Nanomaterials Science & Engineering (NMS&E), Vol.3, No.1, 2021

NANOMATERIALS
SCIENCE & ENGINEERING
Vol. 3, No. 1, pp. 5-13 (2021)

RESEARCH ARTICLE

https://doi.org/10.34624/nmse.v3i1.23923

# Polarization switching in PVDF ferroelectric polymer composites containing graphene layers: molecular dynamic simulations

**V. S. Bystrov[1, *], E.V. Paramonova[1], A.V. Bystrova[1, 2], Hong Shen[3], Xiangjian Meng[3]**

*[1] Institute of Mathematical Problems of Biology, Keldysh Institute of Applied Mathematics, RAS, 142290 Pushchino, Moscow region, Russia*
*[2] Riga Technical University, Kalku Street 1, Riga, LV-1658, Latvia*
*[3] Shanghai Institute of Technical Physics, Chinese Academy of Sciences, Shanghai 200083, China*
**Corresponding author, e-mail address: vsbys@mail.ru*

Received 26 February 2021; accepted 7 March 2021; published online 30 March 2021

## ABSTRACT

The study of composite nanostructure containing ferroelectric polymer PVDF and graphene layers was carried out in this work by molecular modeling methods and the PM3 semi-empirical method of quantum molecular dynamic (MD) calculations using HyperChem software.

It is firstly shown here that the inclusion (addition) of graphene layers to the ferroelectric PVDF polymer increases the coercive field of the composite structure and decreases the polarization switching times of this composite heterostructure. New compositions of such nano- and heterostructures with altered or adjustable times of polarization switching and coercive fields can be constructed based on the obtained calculation results. It provides new opportunities for device constructions such as sensors for nanotechnological and biomedical applications.

## 1. INTRODUCTION

Ferroelectric polymers and polymer films, including based on polyvinylidene fluoride (PVDF) and poly(vinylidene fluoride-trifluoroethylene) (P(VDF-TrFE)), are of considerable interest for various applications due to their convenient and specific properties (piezoelectric and pyroelectric, specially polarization switching) [1-6]. Recently, researchers have been particularly interested in studying their properties at the nanoscale, because these thin and ultrathin PVDF/P(VDF-TrFE) films obtained by the Langmuir-Blodgett (LB) method [6-16] being two-dimensional ferroelectrics [6, 9, 10, 17, 18] demonstrate the phenomenon of polarization switching at the nanoscale with local switching of ferroelectric polarization [6–18], local piezoelectric effect [8-10, 16] and pyroelectric properties in wide-range diapason [13, 18-20]. These properties are extremely important both for understanding the main fundamental processes and phenomena of ferroelectricity at the atomic-molecular level, and for new promising applications in a wide variety of fields of nanosciences and various nanotechnology. Nanomaterials based on ferroelectric polymers can be easily adapted to the production of nanodevices of various geometries, for example, nanolayers, nanofibers, combined heterostructures, etc.

Recently the PVDF/P(VDF-TrFE) and graphene/graphene oxide (G/GO) nanocomposites was made in the form of layers and fibers [21-29]. Such materials demonstrate changes of piezo- and pyro-electric properties depending on concentration of the G/GO components in their structures [20, 27, 28]. These features turn out to be highly important for the creation of new composite materials with adjustable properties.

An important parameter of thin polymer ferroelectrics is also the polarization switching times [18, 19, 30, 31]. Particular interest here is the possibility of using such ultra-thin ferroelectric films in various increasingly miniature nano-devices, switches and sensors. A significant dependence of the polarization switching times on the thickness of the films (the number of layers or unit cells) was established and recently investigated both experimentally and theoretically, using various modeling methods, including molecular dynamics (MD) simulation [30].

It was shown that, within the size *l*, comparable or smaller than the critical domain nuclei *l** ($l \le l^*$) [18, 19], the ferroelectric phenomena in such nanoscale ferroelectrics is fully described by the Landau-Ginzburg-Devonshire (LGD) theory and the polarization switching kinetics is corresponding to Landau-Khalatnikov equations [18, 19, 31]. Near the critical values of the electric field E close to the intrinsic coercive one *Ec*, the dependence of the important switching parameter (switching time $\tau_S$) on electrical field magnitude is determined by the linear relation between square of the inverse switching time $\tau$ and the applied electric field E (for $E > Ec$) according to [31]:

$$1/(\tau)^2 \sim (E - Ec) \qquad (1)$$

The relation (1) allows us to calculate this dependence in the vicinity of the coercive field [17-19].

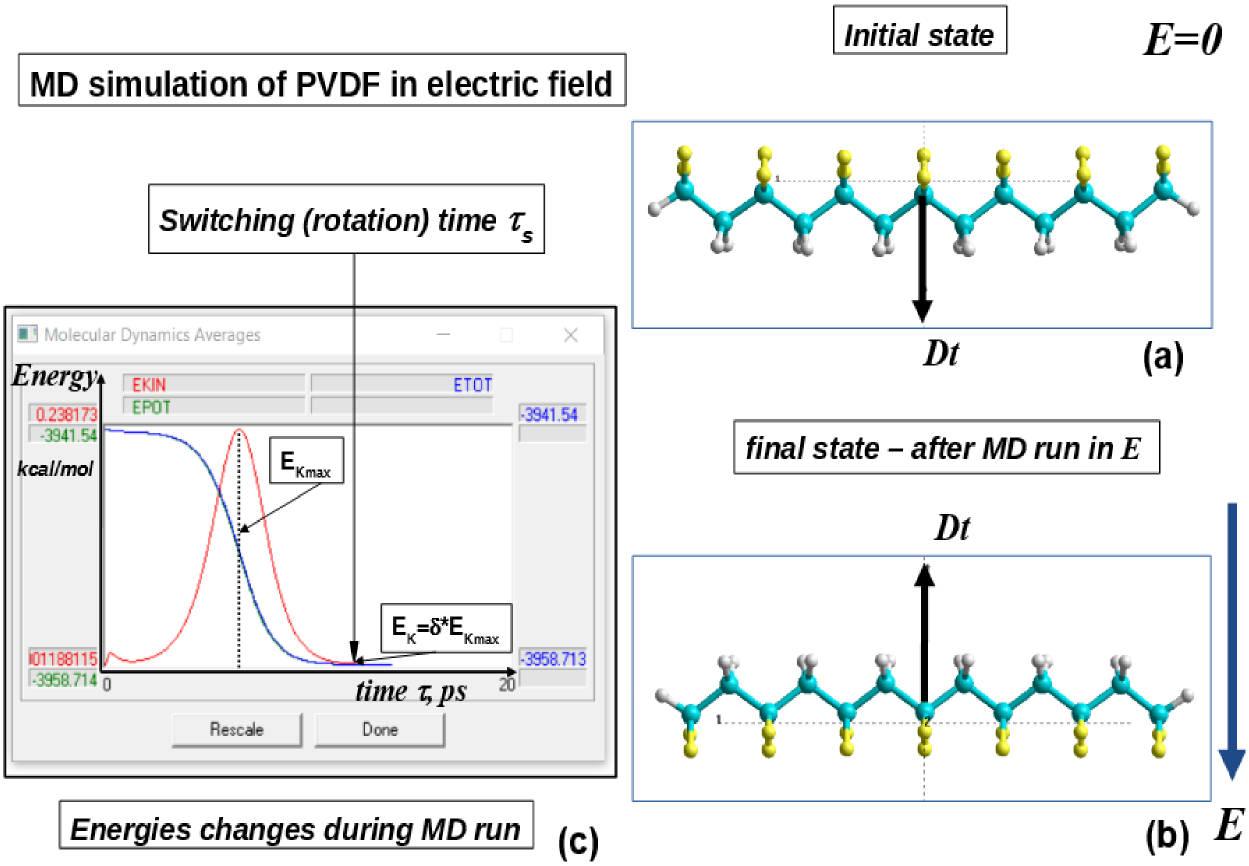

Figure 1. Principles of the molecular dynamics (MD) simulations run (example of PVDF6 chain) using PM3 RHF method calculations by HyperChem software at each MD run step:

(**a**) initial state; (**b**) final state after the MD run with dipole moment ***Dt*** orientation turned (switched) in the opposite direction in the applied electric field E; (**c**) changes of the MD average energies trajectory over time during the MD run (in ps units) and the time of the switching $\tau_S$ for this PVDF system (RED – kinetic energy, BLUE – total energy, GREEN – potential energy). Colour for model: Carbon atom C is CYAN, Fluorine atom F is YELLOW and Hydrogen atom H is GREY.

The influence of graphene layers inclusions on the switching times in composites based on polymer ferroelectrics, has not yet been studied at all. The similar influence of graphene oxide should be investigated too.

Although, this phenomenon is of considerable interest and can determine the properties of newly made composite and hybrid nanomaterials with controlled switching times, which would undoubtedly be very promising for many practical applications. In this research, the dependence of the change in the polarization switching time in thin PVDF film layers on the embedded graphene layer was studied by quantum molecular dynamics methods with quantum chemical semi-empirical calculations at each step of the molecular dynamics run using the HyperChem software [33]. The quantum-mechanical calculations at each step of the MD were carried out using semi-empirical methods PM3 in RHF approximation developed by authors earlier in [17-19, 27-30, 32].

## 2. COMPUTATIONAL METHODS AND MODEL DETAILS

In this work, we used the basic approaches and models developed by us in previous works [17-20, 26-30, 32]. To reveal the main effect of the influence of graphene on the polarization switching times in the polymer ferroelectric PVDF, we considered the model of PVDF as chains of n = 6 basic elementary units $(C_2H_2F_2)_n$. This model is named here as “PVDF6”. Firstly we carried out a study of the polarization switching of such a PVDF6 chain using molecular dynamics (MD) simulation methods, similar to methods used in our previous researches [30] (Fig. 1).

The simulation results are given in comparison with data published in [17-20, 26-30, 32]. These obtained results and main principles of MD simulation are additionally discussed and shown below in section 3.

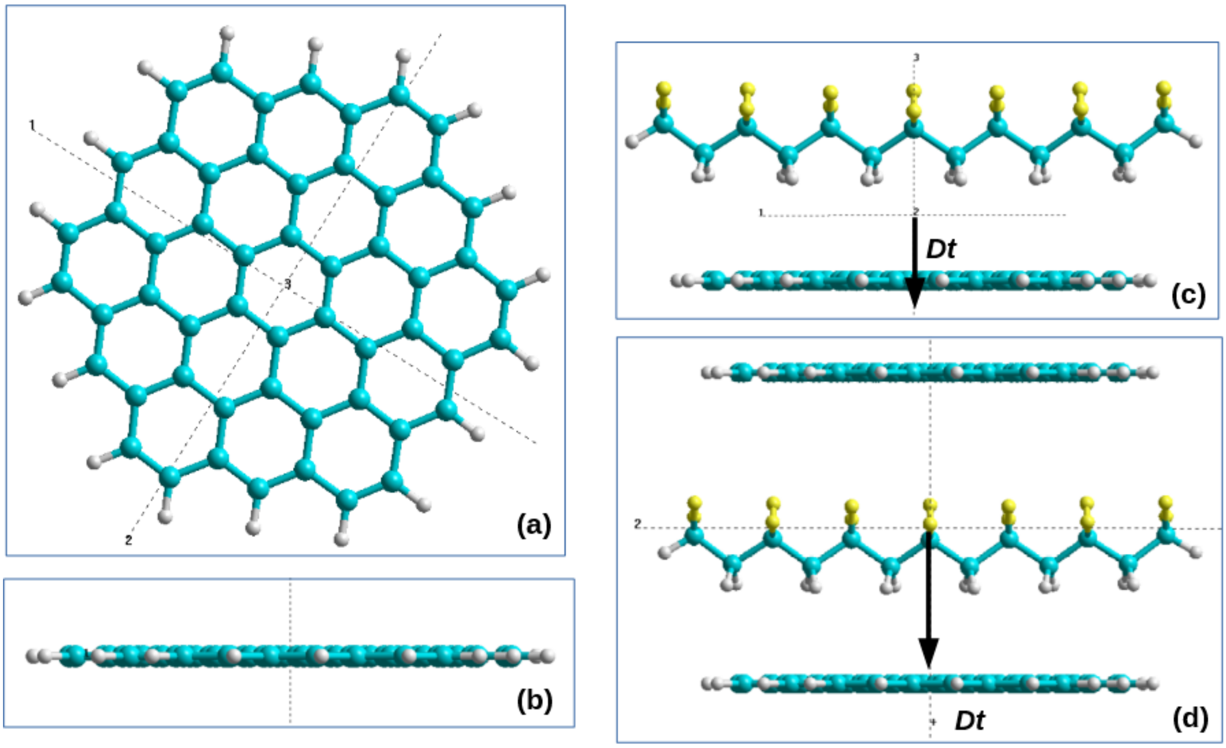

Figure 2. Models of initial states for one Graphene layer and one PVDF6 chain: a) Graphene layer model Gr54H with 54 carbon atoms C (CYAN), arranged round by the hydrogen atoms H (GRAY),

in Z-plane; b) the same in Y-projection plane; c) “PVDF6+G54H_H-C” model in the initial state of PVDF6 chain and Gr54H with “H-C” positions; c) the sandwich structure “Gr54H+PVDF6+Gr54H” model in the initial state. Initial dipole moment ***Dt*** orientation is shown by vector – black arrow.

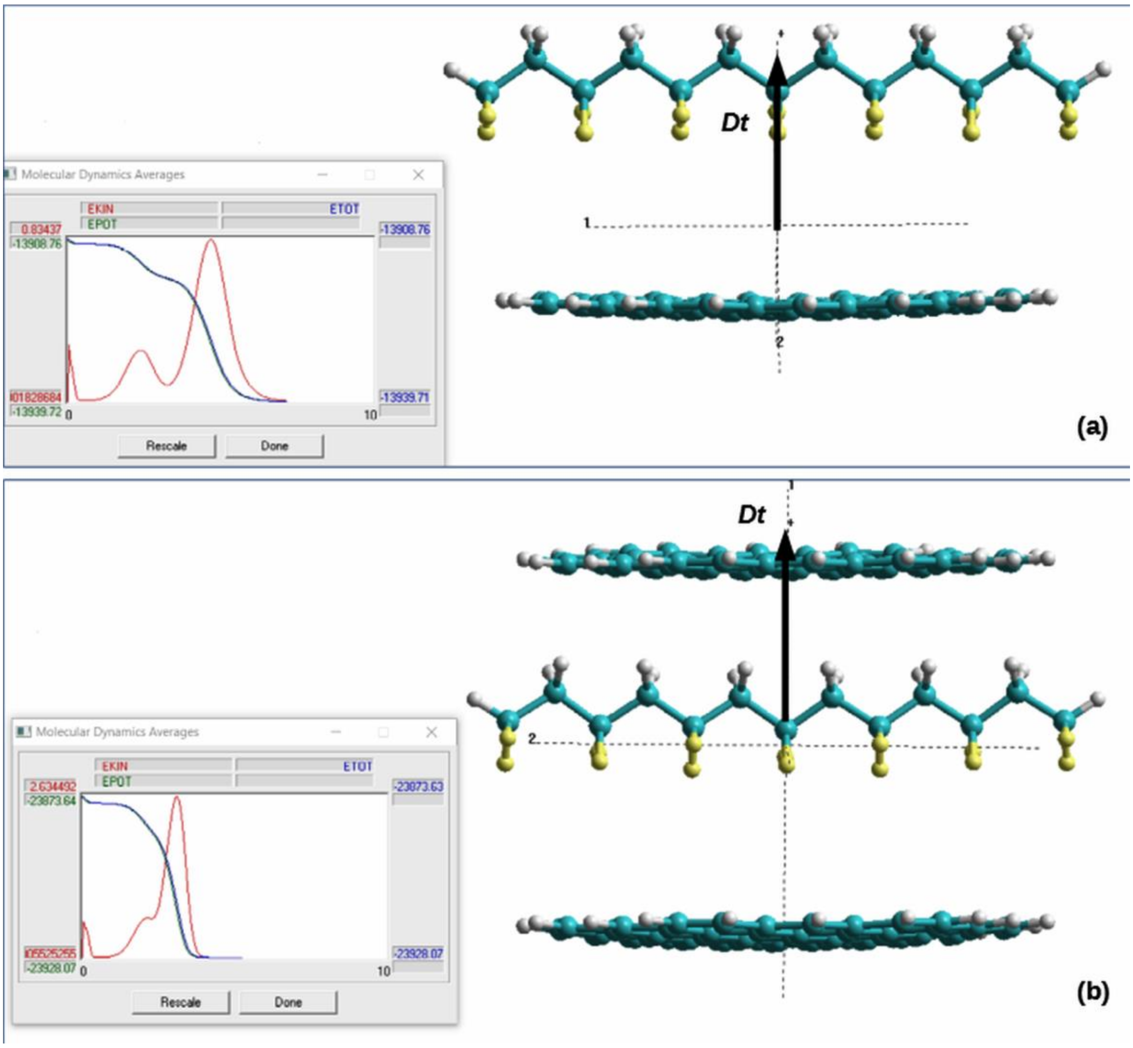

Figure 3. Final states of the “PVDF+Gg54H” models after PVDF chain and total dipole Dt rotation (switching) in the applied electric field E:

a) one-side “PVDF6+G54H_H-C” model with switched opposite orientation of the total dipole moment ***Dt*** in comparison with initial state on Fig. 2 c;

b) sandwich “G54H+PVDF6+G54H” model with the same opposite switched ***Dt*** in comparison with initial state shown on Fig. 2 d. On right side of each pictures shown examples of the MD average energies trajectory over time during the MD run similar as on Fig. 1.

Further, the model of the graphene layer developed earlier will be used [24, 25, 27, 29]. This simplest model consists of 54 carbon C atoms surrounded on the edge by hydrogen atoms H [29] (Fig. 2 a, b). This model is named here as “Gr54H”.

We consider two types of the models as the main composite (hybrid) structures “PVDF6+Gr54H”:

1) one-sided model “PVDF6+G54H_H-C”, where the PVDF chain (or layer) is directed to the graphene layer by hydrogen atoms H (Fig. 2 c);

2) two-sided model (or sandwich model) “G54H+PVDF6+G54H”, where the PVDF chain (or layer) is surrounded on both sides by two graphene layers (Fig. 2 d).

This model construction approach is similar to the model, which we used for calculating the piezoelectric coefficients of similar PVDF and graphene composites [28, 29].

The semi-empirical PM3 method in the restricted Hartree-Fock (RHF) approximation [32, 33] was used for the quantum calculations of the initial structures of all models and for calculations

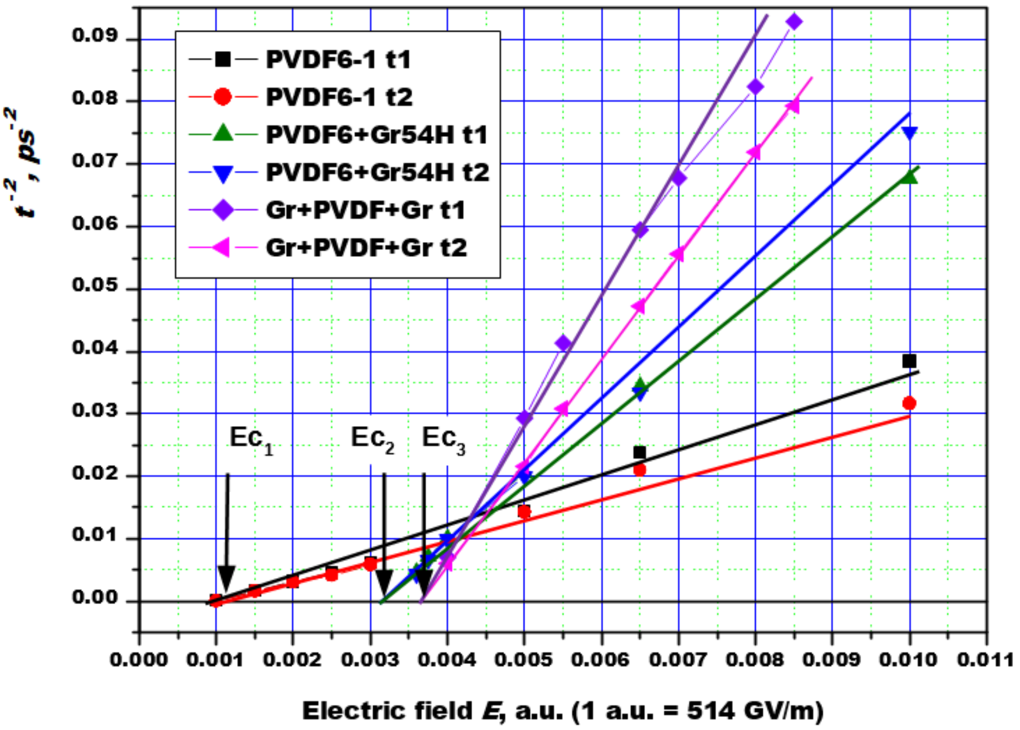

Figure 4. Square of the inverse switching time $\tau$ (1) as a linear function of the electric field E for different models, taking into account the spread of data accuracy between the values of t1 and t2.

during the MD run at each of its steps. This PM3 method is included in the HyperChem package [33].

The main part of all quantum-chemical calculations in HyperChem was made using Single Point (SP) calculation method. For cases of the hysteresis loop calculations, when is necessary to take into account the changes of geometry of the molecular systems, the optimization of molecular systems and finding of their optimal geometry is performed using the Polak–Ribere (conjugate gradient method) algorithm, included in HyperChem package [33]. This approach is especially important for the case of the dipole moment rotation switching (and polarization switching) in the applied electric field at the critical point of the systems. Simulation of the system under an imitated applied constant electric field is available in HyperChem packages too [33].

The main approach used in this work is MD simulation run and changes of the modelled structures under applied electric field ***E*** with its various values using HyperChem software [33]. Performing of such MDS calculations and runs requires specifying a certain set of parameters, which are set in the MD option of the HyperChem program. The main initial parameters are following: MD calculations perform at constant temperature (for each used electric field value) in vacuum, with bath relaxation time = 0.05 ps; for MD run parameter “run time” = 5 – 20 ps (depending of necessary time interval, in which switching process observed) and with “step size” = 0.0005 – 0.001 ps, which is varied depending of applied electric field and the rate of the molecular chain rotation.

## 2. MAIN RESULTS AND DISCUSSIONS

Results of MD run calculations obtained for various electric field applied values E, directed opposite the electric field arisen by the PVDF dipole moment vector, show that during this MD run the PVDF

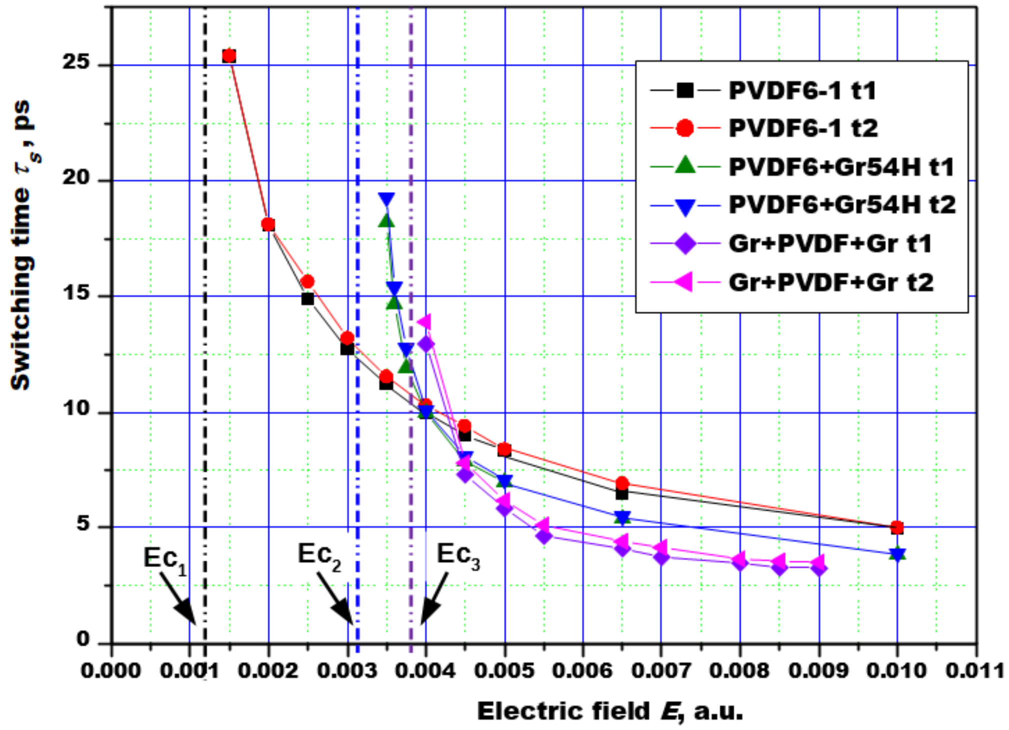

Figure 5. Behaviour of the switching time $\tau$ (1) as a function of the electric field E for different models, taking into account the spread of data accuracy between the values of t1 and t2.

chain and its total dipole ***Dt*** turn gradually so, that it eventually rotates in the opposite direction in the final state. As results, all initial models (shown on the Fig. 1 a, Fig. 2 c, d) undergo different structural changes under the influence of electric fields of different magnitudes - rotation of the PVDF dipole structure is performed with different speeds depending of the electric field value. Some examples of the final states of different considered models after a such flipping (switching) are shown in Fig. 1 b, Fig. 3.

The corresponding changes of all MD average energies with time are shown as example in Fig.1c. The final time of two-chain rotation (switching time $\tau$) was estimated from these MD energies trajectories at the criteria $\delta \sim E_K/E_{Kmax} \leq 0.01 - 0.001$, where $E_K$ is the kinetic energy at the final point and $E_{Kmax}$ is the kinetic energy at the maximum of the chain rotation (as shown in Fig. 1 c). The calculated data and performed MD run in various electric field show clearly the different behaviour of the PVDF chain at the strong and at the low electric field and allow us to obtain the critical behaviour at the electric field $E \sim Ec$ at the low limit of this electric field, $E \rightarrow Ec$ for $E > Ec$.

Results of the switching time $\tau$ variations obtained from MD run calculations for various electric field values ***E*** are presented below on Fig. 4 and Fig. 5. The data obtained is very interesting.

First, the behaviour of the PVDF chain alone was considered (Fig. 1 c, d). It is in good comparison with previous calculations [17-19, 30] shown a linear behaviour (1) with coercive field *Ec* ~ 0.5 GV/m (Fig. 4).

Second, the behaviour of one-side heterostructure “PVDF6+G54H_H-C” model was investigated (Fig. 3 a, Fig. 4, Fig 5). The result showed that the rotation (switching) time $\tau_s$ became shorter, that is, the rotation is faster under the influence of the graphene layer. The coercive field is increased up to *Ec* ~ 1.5 GV/m.

On the other hand, it is interesting and important that in this case the graphene layer itself does not

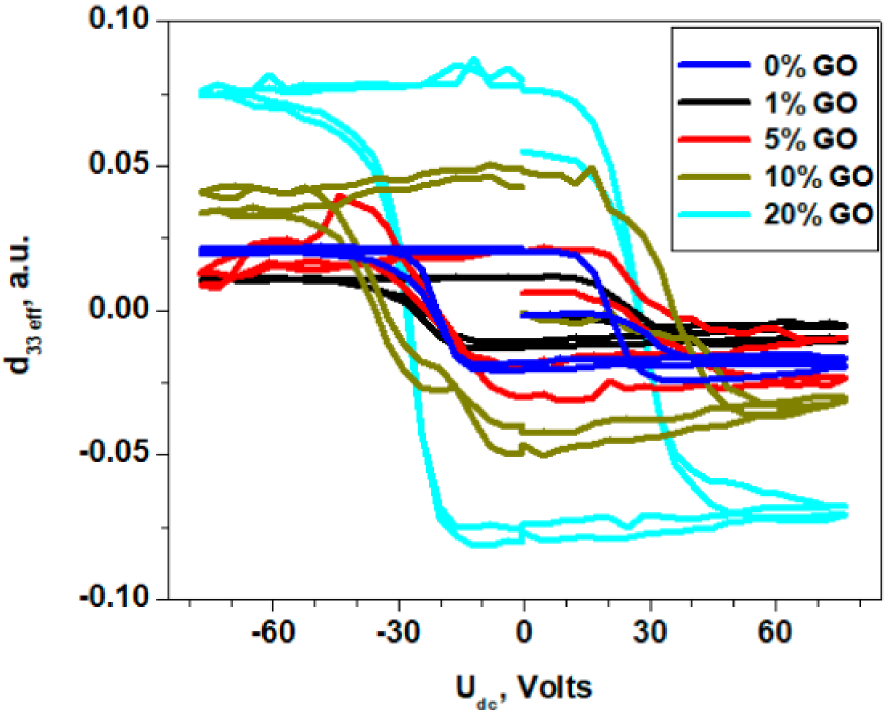

Figure 6. Piezoresponse hysteresis loops of P(VDF-TrFE)-graphene oxide fibers with different concentration of GO. *U*ac = 7.5 V, 40 kHz (data from [25]).

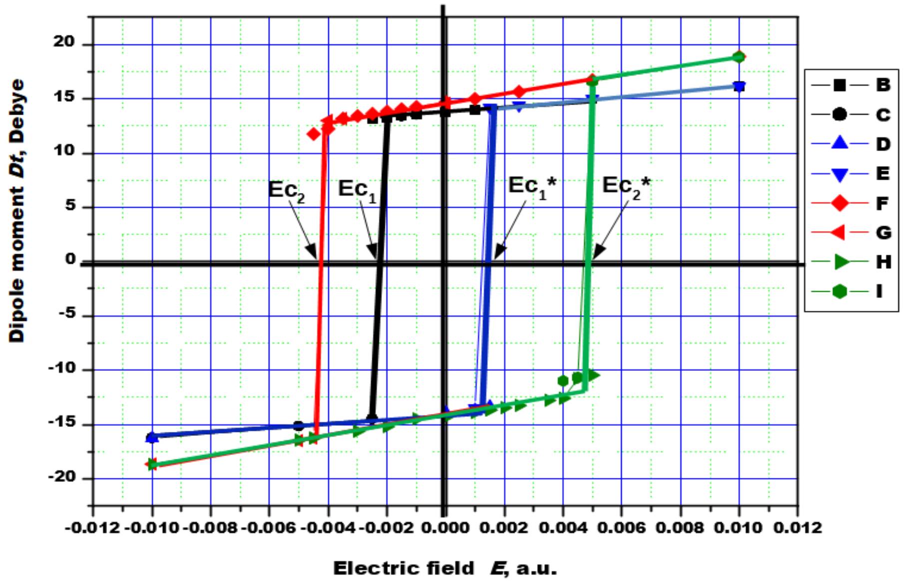

Figure 7. Calculated hysteresis loop of PVDF6 model (B-C down, D-E up branches) and for "PVDF6+G54H_H-C" model (F-G down, H-I up branches) with increased coercive field *Ec*: from $Ec_1$ up to $Ec_2$ for left side and from $Ec_1$* up to $Ec_2$* for right side (due to some asymmetry of hysteresis loop for various electric field direction in relation to the $C_2H_2F_2$ dipoles in PVDF6 chain).

overturn, but mainly retains its previous position. Rotated only PVDF chain.

Third, the behaviour of the sandwich "Gr54H+PVDF6+Gr54H" hetero-structure shows even shorter switching times (Fig. 3 b, Fig. 4, Fig. 5) and increasing of coercive field up to *Ec* ~ 2 GV/m.

Thus, the calculations performed by the quantum MD simulation method show that, under the influence of graphene layers, the switching times $\tau$ in the ferroelectric PVDF polymer decrease and coercive field *Ec* increase. And this can have important technological and practical implications and applications.

It should also be noted the fact that in the works [24, 25], in which the properties of the similar composite “PVDF + Graphene”, but some more complex composition (with Graphene oxide and P(VDF-TrFE)), were studied - and it was found that the addition of graphene/graphene oxide increases the value of the coercive field in comparison with the pure polymer composition (Fig. 6).

Moreover, with an increase in the graphene concentration, this shift towards an increase in the coercive field value increased more and more (up to a certain level of graphene concentration) (Fig. 6).

This fact is confirmed in our presented calculations (Fig. 4, 5).

In addition to calculating the switching times, here we calculated the hysteresis loop of pure PVDF and the hysteresis loop for the PVDF + Gr54H (H-C) model (Fig. 7) and obtained a clear increase in the width of the hysteresis loop, that is, an increase in the value of the coercive field, under the influence of the addition of graphene layer.

## 5. CONCLUSIONS

The calculations and MD simulations presented in this article unambiguously show that the coercive field increases and the polarization switching time decreases under the influence of graphene layers in thin layers of polymer ferroelectrics. These results of modeling and calculations, of course, require experimental verification. This can be done directly by production of samples of the type of PVDF layers deposited by the LB method on graphene layers or similar hetero-structures (of different thicknesses and / or different numbers of layers - similar, for example, to the work [13]). Following measurements of the hysteresis loops and switching times (similar to the works of the [12-16]) of these samples could be done for the proceeded experimental verification of obtained in this work results.

The results of performed investigation are undoubtedly important and relevant, since they demonstrate the direction of the necessary structural modifications of newly produced nanomaterials with predetermined and desired properties. In this case, we get the opportunity to regulate and control the switching times and the magnitude of the coercive field, which are extremely important parameters for new designed nanodevices (for example, memory devices or switching sensors) based on polymer ferroelectrics and graphene/graphene oxide layers and similar two-dimensional heterostructures.

## ACKNOWLEDGMENTS

The authors are greatly thankful to the Russian Foundation for Basic Researches (RFBR): grant # 20-51- 53014_ A.

A.V. Bystrova is grateful to the Riga Technical University for the RTU Doctoral Studies 2019/2020, academic year grant No. 04000-1.1-e/12.

Xiang-Jian Meng expresses his gratitude to the National Natural Science Foundation of China (NNSFC) for the grant # 61574151 and Hong Shen for the grant # 62011530043.

## REFERENCES

[1] M. E. Lines, A. M. Glass. Principles and Applications of Ferroelectrics and Related Materials. Oxford: Clarendon (1977).

[2] T. T. Wang, J. M. Herbert, A. M. Glass. The Applications of Ferroelectric Polymers. New York: Chapman and Hall (1988).

[3] H. S. Nalwa. Ferroelectric Polymers. New York: Marcel Dekker (1995).

[4] A. K. Tagantsev, L. E. Cross, J. Fousek. Domains in Ferroic Crystals and Thin Films. New York: Springer (2010). 821 p.

[5] J.F. Scott, Ferroelectric Memory, Berlin: Springer (2000).

[6] V. Fridkin, S. Ducharme. Ferroelectricity at the Nanoscale. Basics and Applications. Berlin: Springer-Verlag (2014).

[7] S. Palto, L. Blinov, A. Bune, E. Dubovik, V. Fridkin, N. Petukhova, K. Verkhovskaya, S. Yudin. Ferroelectric Langmuir-Blodgett films. Ferroelectric Letters, **19**, 65–68 (**1995**).

[8] A.V. Bune, Ch. Zhu, S. Ducharme, L. M. Blinov, V. M. Fridkin, S. P. Palto, N. G. Petukhova, S. G. Yudin. Piezoelectric and pyroelectric properties of

ferroelectric Langmuir-Blodgett polymer films. *J. Appl. Phys.*, **85**, 7869 (1999).

[9] A. V. Bune, V. M. Fridkin, S. Ducharme, L. M. Blinov, S. P. Palto, A. V. Sorokin, S. G. Yudin, A. Zlatkin. Two-dimensional ferroelectric films. Nature (London), **391**, 874-877 (1998).

[10] L.M. Blinov, V.M. Fridkin, S.P. Palto, A.V. Bune, P.A. Dowben, S. Ducharme, Two-dimensional ferroelectrics, *Physics-Uspekhi*, **43**, 243–257 (2000).

[11] H. Qu, W. Yao, J. Zhang, S. Dusharme, P. A. Dowben, A. V. Sorokin, V. M. Fridkin. Nanoscale polarization manipulation and conductance switching in ultrathin films of a ferroelectric copolymer. *Appl. Phys. Lett.*, **82** (24), 4322–4324 *(*2003).

[12] H. Kliem and R. Tardos-Morgane. Extrinsic versus intrinsic ferroelectric switching: experimental investigations using ultra-thin PVDF Langmuir-Blodgett films. *J. Phys.: D Appl. Phys*., **38,** 1860-1868 (2005).

[13] J. L. Wang, B. L. Liu, X. L. Zhao, et al. Transition of the polarization switching from extrinsic to intrinsic in the ultrathin polyvinylidene fluoride homopolymer films. *Appl. Phys. Lett*., **104**,182907 (2014).

[14] R. V. Gaynutdinov, S. Mitko, S. G. Yudin, V. M. Fridkin, S. Ducharme. Polarization switching at the nanoscale in ferroelectric copolymer thin films. *Appl. Phys. Lett*., **99**, 142904 (2011).

[15] R. Gaynutdinov, S. Yudin, S. Ducharme, V. Fridkin, V. Homogeneous switching in ultrathin ferroelectric films. *J. Phys. Condens. Matter*, **24**, 015902 (2012).

[16] V. S. Bystrov, I. K. Bdikin, D. A. Kiselev, S. G. Yudin, V. M. Fridkin, A. L. Kholkin. Nanoscale polarization pattering of ferroelectric Langmuir-Blodgett P(VDF-TrFE) films. *J. Phys. D: Appl. Phys*., **40**, 4571–4577 (2007).

[17] V. S. Bystrov, V. M. Fridkin. Two-dimensional ferroelectrics and homogeneous switching. To the 75th anniversary of the Landau—Ginzburg theory of ferroelectricity. *Phys. Usp*., **63,** 417–439 (2020).

[18] E. Paramonova, V. Bystrov, Xiangjian Meng, Hong Shen, Jianlu Wang, V. Fridkin. Polarization switching in 2D nanoscale ferroelectrics: Computer simulation and experimental data analysis. *Nanomaterials*, **10** (9), 1841 (2020).

[19] E.V. Paramonova, S.V. Filippov, V.E.Gevorkyan, L.A. Avakyan, X.J.Meng, B.B. Tian, J.L. Wang and V.S. Bystrov. Polarization switching in ultrathin polyvinylidene fluoride homopolymer ferroelectric films. *Ferroelectrics*, **509**, 143–157 (2017).

[20] V. S. Bystrov, I. K. Bdikin, M. V. Silibin, X. J. Meng, T. Lin, J. L. Wang, D. V. Karpysky, A. V. Bystrova, E. V. Paramonova. Pyroelectric properties of the ferroelectric composites based on the polyvinylidene fluoride (PVDF) with graphene and graphene oxide. *Ferroelectrics*, **541** (1), 17-24 (2019).

[21] S.-H. Bae, O. Kahya, B.K. Sharma, J. Kwon, H.J. Cho, B. Özyilmaz, J.-H. Ahn. Graphene-P(VDF-TrFE) multilayer film for flexible applications. ACS Nano, **7** (4), 3130–3138 (2013).

[22] R. Md Ataur, L. Byung-Chul, P. Duy-Thach, C. Gwiy-Sang. Fabrication and characterization of highly efficient flexible energy harvesters using PVDF–graphene nanocomposites. *Smart Mater. Struct*., **22** (8), 085017 (2013).

[23] M. M. Abolhasani, K. Shirvanimoghaddam, M. Naebe. PVDF/graphene composite nanofibers with enhanced piezoelectric performance for development of robust nanogenerators. *Compos. Sci. Technol.*, **138**, 49–56 (2017).

[24] M. V. Silibin, V. S. Bystrov, D. V. Karpinsky, et al. Local mechanical and electromechanical properties of the P(VDF-TrFE)-graphene oxide thin films. *Applied Surface Science*, **421,** Part A, 42-51 (2017).

[25] M. Silibin, D. Karpinsky, V. Bystrov, D. Zhaludkevich, M. Bazarova, P. M. Vaghefi, P. A. A. P. Marques, B. Singh and I. Bdikin. Preparation, Stability and Local Piezoelectrical Properties of P(VDF-TrFE)/Graphene Oxide Composite Fibers. *C - Journal of Carbon Research*, **5**(3), 48 (2019). (Special Issue Carbon Nanostructures for Biological Applications).

[26] V.S. Bystrov, I. K. Bdikin, M. V. Silibin, D. V. Karpinsky, S. Kopyl, G. Goncalves, A. Sapronova, T. Kuznetsova, V. V. Bystrova. Graphene/graphene oxide and polyvinylidene fluoride polymer ferroelectric composites for multifunctional applications. *Ferroelectrics*, **509**, 124–142 (2017).

[27] V. S. Bystrov, M. V. Silibin, Xiangjian Meng, Tie Lin, Hong Shen, Bobo Tian, Jianlu Wang, D. V. Karpynsky, A. V. Bystrova, E. V. Paramonova. Modelling of the Piezoelectric and Pyroelectric properties of the Ferroelectric composites thin films based on the polyvinylidene fluoride (PVDF) with Graphene and Graphene Oxide layers and fibers. *Nanomaterials Science and Engineering*, **2 (2)**, 83-92 (2020).

[28] V. S. Bystrov, E. V. Paramonova, I. K. Bikin, A. V. Bystrova, R. C. Pullar, A. L. Kholkin. Molecular modeling of the piezoelectric effect in the ferroelectric polymer poly(vinylidene fluoride) (PVDF). *J. Mol. Model.*, **19**, 3591–3602 (2013).

, S. Kopyl, E. V. Paramonova, G. Goncalves. Molecular modeling of the piezoelectric properties in the Graphene/Graphene oxide and polyvinylidene fluoride (PVDF) polymer ferroelectric composites. *J. Mol. Model*., **23**, 128 (2017).

[30] V. S. Bystrov. Molecular modeling and molecular dynamics simulation of the polarization switching phenomena in the ferroelectric polymers PVDF at the nanoscale. *Physica B: Condensed Matter*., **432,** 21–25 (2014).

[31] G. Vizdrik, S. Ducharme, V. M. Fridkin, S. G. Yudin. Kinetics of ferroelectric switching in ultrathin films. *Phys. Rev. B.*, **68**, 094113 (2003).

[32] V. S. Bystrov, N. K. Bystrova, E. V. Paramonova, G. Vizdrik, A. V. Sapronova, M. Kuehn, H. Kliem, A. L. Kholkin. First principle calculations of molecular polarization switching in P(VDF-TrFE) ferroelectric thin Langmuir-Bliodgett films. *J. Phys: Condens. Matter.*, **19**, 456210 (2007).

[33] HyperChem, Versions 8.0/01, Tools for Molecular Modeling; Gainesville, FL, USA: Hypercube Inc. (2010). Available online: http://www.hyper.com/?tabid=360 (accessed on 7 February 2021).

**NANOMATERIALS**
**SCIENCE & ENGINEERING**
Vol. 3, No. 1, pp. 14-21 (2021)

RESEARCH ARTICLE

https://doi.org/10.34624/nmse.v3i1.23956

# Method for determining the chirality sign of peptide nanotubes using the dipole moments vectors calculations

**V. S. Bystrov[1, *], A. E. Sidorova[2], A. O. Lutsenko[2], D. K. Shpigun[2], V. A. Tverdislov[2], P. S. Zelenovskiy[3,4], S. A. Kopyl[4], A. L. Kholkin[4]**

*[1]Institute of Mathematical Problems of Biology, Keldysh Institute of Applied Mathematics, RAS, 142290 Pushchino, Moscow region, Russia*
*[2]Department of Biophysics, Faculty of Physics, Lomonosov Moscow State University, Moscow, 119991, Russia*
*[3]School of Natural Sciences and Mathematics, Ural Federal University, Ekaterinburg 620000, Russia;*
*[4]Department of Physics & CICECO - Aveiro Institute of Materials, University of Aveiro, 3810-193 Aveiro, Portugal*
**Corresponding author, e-mail address: vsbys@mail.ru*

Received 3 March 2021; accepted 17 March 2021; published online 30 March 2021

## ABSTRACT

In this work the method for calculating the index and sign of chirality using the values of the dipole moments of each individual dipeptides forming a helix structure of a peptide nanotube is proposed.

Calculations of the individual dipeptide dipole moments using semi-empirical quantum method PM3 and force field method Amber are preformed in the frame of HyperChem software package.

Results obtained for diphenylalnine (FF) peptide nanotube (PNT) with two different initial chirality L-FF and D-FF shows correct results of the chirality changes on D and L for helical PNT, corresponding to the law of the change in the sign of chirality, when the hierarchical structure of the molecular system becomes more complex.

The results obtained give us a new opportunity to see the physical basis for the formation of the type and sign of chirality and open up new possibilities for a quantitative study of this phenomenon. This approach can be applied to other similar structures and peptide nanotubes based on other amino acids and dipeptides.

## 1. INTRODUCTION

Amino acids form the basis of many complex biomolecular structures and systems in biology, medicine and modern nanotechnology. They form spiral (helix) self-organizing structures of different levels of hierarchical organization [1]. Among them, the simplest and most energetically favorable are $\alpha$-helices - in biology, this is a common type of regular secondary structure of proteins [1-3]. Moreover, in biology, these helical polypeptide structures of proteins are composed mainly of amino acid residues of left chirality - L-aminoacids [2]. This homochirality of biological systems has developed here, apparently, evolutionary and its reasons are still not clear, although there are a number of hypotheses [4].

But it is important that for natural proteins from these L-aminoacids the regular alternation of the sign (or type) of chirality from the left type “L” to the right type “D” begins in structures of different levels of hierarchical organization: L-D-L-D [5-8]. Accordingly, a biological reproduction system based on DNA has a parallel sequence of changes in the chirality of D-L-D-L with increasing complexity of their level of organization. Research by V.A. Tverdislov’s group from Moscow State University [5-8] showed that this property of chirality is a key point in the hierarchy and self-organization of biological systems.

It should be noted that the very concept of chirality is a general property of an object - not to overlap with its mirror image; so the left and right hand do not match in the mirror. This universal property of matter can be observed at various hierarchical levels from subatomic, molecular and supramolecular scales [9-11]. And not only in living biological systems, but also in many related structures based on the same initial amino acids, artificial and self-organizing molecular structures with various bionanotechnological applications. And here, in principle, left L and right D amino acids can be present on equal terms, while providing a difference in the physical and chemical properties of the structures formed on their basis. This also turns out to be very important for pharmacology and the like.

One of the examples of such self-organizing macromolecular systems are peptide nanotubes (PNT) based on the amino acid phenylalanine (Phe or F) and its dipeptide, diphenylalanine (FF, or in its usual aqueous zwitterionic form H-FF-OH) [11–20]. Possessing a wide range of useful properties, these structures are promising for various applications in nanotechnology, nanoelectronics, and biomedicine [14-16]. Self-assembly of such PNTs occurs in aqueous media rather quickly and under certain conditions affecting the rate of their growth, the shape of self-organizing structures (their thickness and length), and their physical properties [21].

Despite the increasingly widespread use of the concept of chirality in various fields, the assessment of the sign of chirality has so far been mainly qualitative. There is an urgent need for a quantitative assessment of the magnitude and sign of chirality.

Just recently, in the works of a group of the Department of Biophysics, Moscow State University, a simple and clear method for calculating chirality was proposed, based on a strict quantitative calculation of the mixed vector product of three consecutive vectors connecting the central carbon atoms of Ca of neighbouring amino acids of the polypeptide helical structures [22-24]. This approach has already been tested by authors of these works on a wide variety of proteins taken from the Protein Data Bank [25]. These approaches are described in detail in the mentioned works.

In this work, we propose a similar approach, but based on other vectors, namely, on the vectors of the dipole moments of individual amino acids that form the peptide sequence of such $\alpha$-helix. Here, as an example, we use the structures of peptide nanotubes (PNT) forming $\alpha$-helices of different types of chirality D and L based on self-assembly from solutions of di-phenylananine (FF) dipeptides of different initial chiralities L-FF and D-FF.

These PNTs were recently investigated in detail experimentally and by methods of computer simulation and calculations, using various approaches - quantum chemical and density functional theory methods [26, 27], including using the VASP program [28]. These studies made it possible to identify sets of sequential vectors of individual dipole moments on the turn of each helix of different types of chirality. To calculate the dipole moments, we used the HyperChem software package [29], which includes an extensive set of different methods: molecular mechanics, molecular dynamics, and various quantum mechanical methods, including semi-empirical quantum methods of various parametrization (AM1, PM3, RM1, etc.) in the Hartree-Fock approximation (restricted and unrestricted). Using these results, in this work, the chirality index is calculated using a technique similar to that proposed and developed in [22-24], but for vectors of dipole moments.

It should be noted that these nanotubes (as well as many similar self-organizing peptide molecular nanostructures in general, based on ordered periodic molecular-crystal structures), well experimentally recorded by modern X-ray methods, and accumulated in the well-known crystallographic Cambridge database CDCC [30], in somewhat similar to the protein database [25]. However, they are not formed on the basis of individual single amino acid residues, but their dipeptides, that is, pairs of amino acids. Depending on the conditions of self-assembly (the type of solution and other factors), they can form both $\alpha$-helices and $\beta$-sheet [16, 17], the latter being characteristic of Anzheimer's disease. In this case, the right D-FF dipeptides obtained in the experiment have the initial $\alpha$-helix structure (a-helix) and form a left type $\alpha$-helix - “L”, while the initially left L-FF dipeptides have the structure named as “left-handed helix” [11] and form a right-type $\alpha$-helix - “D”.

Our task is to carry out calculations using the known dipole moments of each individual dipeptide, arranged sequentially along a turn in the structure of nanotubes with their own different chiralities (for one turn, one turn in a helix (spiral) - 6 such dipeptides is put here).

It is important here to choose the right basis and orientation of the coordinate axes - for left and right nanotubes.

## 2. COMPUTATIONAL METHODS AND MODEL DETAILS

In this work the models of the diphelylalanine (FF) peptide nanotubes (PNT) with different chirality D-FF and L-FF were constructed using the experimental X-ray data obtained from the Cambridge Crystallographic Data Centre (CCDC) crystallographic database [30] and transformed to the workspace of the HyperChem software [29]. The full details of the FF PNT α-helix constriction on the HyperChem workspace is described in our work [19]. These using data correspond to L-FF was taken from Görbitz work [13] (placed at the No. CCDC 16337 on [30]); and for D-FF was taken from recently reported in the paper [20] (deposited in the CCDC [30], at the No. CCDC 1853771).

For calculation of dipole moment of each FF dipeptides as well as the total dipole moment of both L-FF and D-FF PNT α-helix the semi-empirical quantum-mechanical (QM) method PM3 in the restricted Hartree-Fock approximation (RHF) and molecular mechanical (MM) force field method Amber from HyperChem package [29] were used in this work similarly as in works [18-20].

In these studies were shown that main features of the other methods used (such as AM1 and BIO CHARM) give in these cases approximately the same results of the dipole moments and energy calculations. Therefore, now in this work we use only PM3 and Amber. All calculated dipole moment data are presented in Debye units in this HyperChem software.

To evaluate and calculate the index and sign of chirality, in this work is proposed to use a *mixed (or vector-scalar) product* of three successive vectors of dipole moments ***D**ᵢ* produced by individual FF dipeptides constituting the α-helix PNT coil. This approach is similar to the method for evaluating the sign and measure of chirality of the protein helical structures recently developed in [22-24]. The essence of this method is as follows. A model of a polypeptide chain consisting of *n* amino acid residues and having, respectively, *n* $C_\alpha$ atoms - reference points in the method is considered. Vectors $v_i$ are built between each two adjacent reference points, and then for each three consecutive vectors their mixed (scalar vector) product is calculated (taking into account their coordinates):

$$([v_1, v_2], v_3) = (y_1 z_2 - y_2 z_1) x_3 + (z_1 x_2 - z_2 x_1) y_3 + (x_1 y_2 - x_2 y_1) z_3 \ , \qquad (1)$$

The sum of all mixed products allows us to estimate the sign of chirality

$$\chi_{total} = \sum_{i=1}^{n-3} ([v_i, v_{i+1}], v_{i+2}), \qquad (2)$$

If the structure is right-handed, then the mixed products will be positive and the chirality value will also be positive, and for left-handed structures - negative. The mixed product was normalized to a certain degree of the average length of the vectors used (a cylindrical helical line with evenly spaced points was taken as a standard). This made it possible to obtain a quantitative characteristic of the normalized value of chirality:

$$\chi_{norm} = \sum_{i=1}^{n-3} \frac{([v_i, v_{i+1}], v_{i+2})}{C_i} \qquad (3)$$

where $C_i$ is the normalization factor.

The method is implemented as a computer program in Python 3.7 and has been validated for over 700 proteins.

In this work we provide the calculation of the sign of the chirality for diphenylalanine (FF) PNT based on dipeptides of different initial chirality (L-FF and D-FF). Using the approach similar [24], and applying it to the vectors of dipole moments of the each individual dipeptides $\boldsymbol{D_{t,i}}$ with its module of total dipole momentum

$$\boldsymbol{D_{t,i}} \ (D_{t,i} = \sqrt{D_{x,i}^2 + D_{y,i}^2 + D_{z,i}^2},$$

where $D_{t,\,i}$ is the total dipole moment of the *i*-th dipeptide vector in the α-helix structure of the PNT; $D_{x,\,i}$, $D_{y,\,i}$, $D_{z,\,i}$ are the components of the *i*-th vector

$\boldsymbol{D}_{t,\,i}$ in the Cartesian coordinates; we can write down the chirality index of the helical structures $c_{total}$ ; and for the normalized chirality - $c_{norm}$:

$$c_{total} = \sum_{i=1}^{n-2}\left(\left[D_{t,i}, D_{t,i+1}\right], D_{t,i+2}\right),\quad c_{norm} = \frac{c_{totalL}}{\left(D_{t,i}^{av}\right)^{3}} \qquad (4)$$

To calculate these data of the chirality index we must to compute data for all individual FF dipole moment and obtain a full set of these dipoles momentum data.

## 3. MAIN RESULTS AND DISCUSSIONS

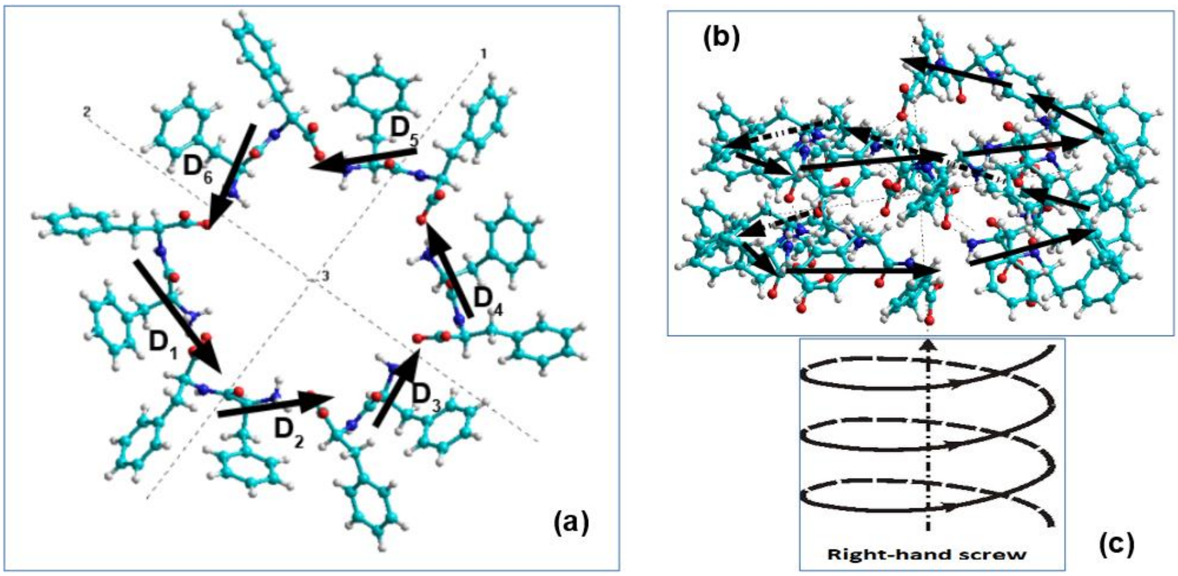

Figure 1. Schematic representation of the spatial distribution of FF individual dipole moments $\boldsymbol{D}_i$ ($\boldsymbol{D}_{t,i}$ in (4)) for two coils of the PNT $\alpha$-helix of L-FF chirality conformation structure forming right-hand screw D.

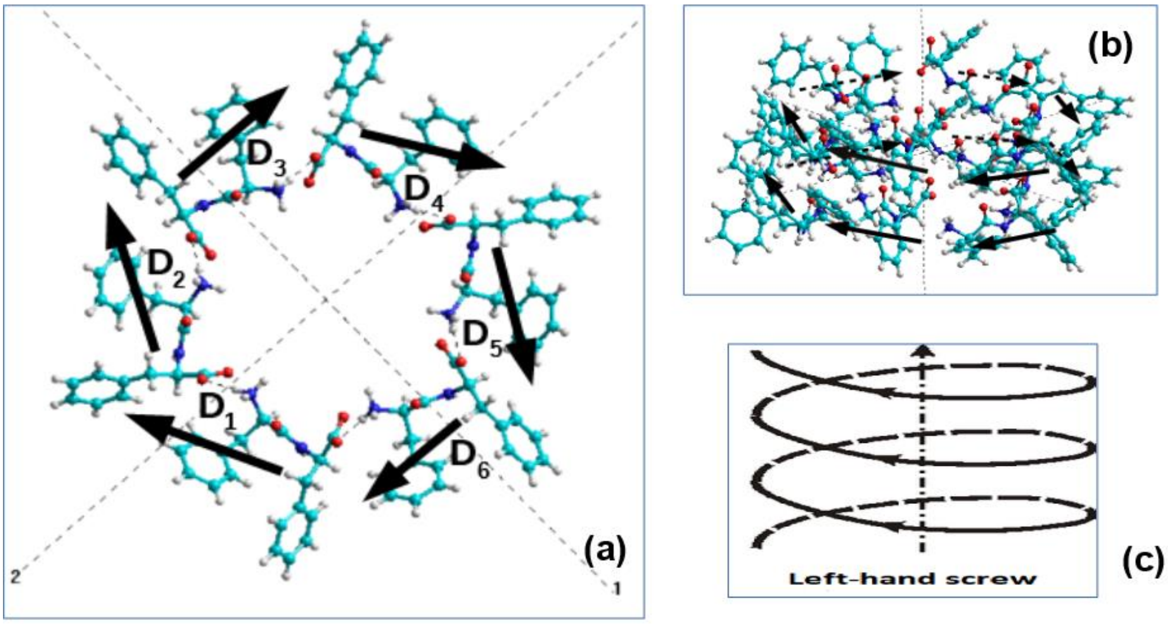

Figure 2. Schematic representation of the spatial distribution of FF individual dipole moments $\boldsymbol{D}_i$ ($\boldsymbol{D}_{t,i}$ in (4)) for two coils of the PNT $\alpha$-helix of D-FF chirality conformation structure forming left-hand screw L.

Table 1. Dipole moments data for **L-FF PNT,** computed using QM **PM3 RHF** and MM **Amber** methods for 2-turns (coils) model structure of L-FF PNT, obtained on the experimental structural X-ray data. All values of dipole moments are given here in **Debye** units.

(Data presented are for one upper turn, containing 6 FF molecules, from 2 turns of $\alpha$-helix L-FF PNT model, stacked in one period of PNT structure along the c axis).

| # | **PM3 RHF** | | | | **Amber (BIO CHARM) after PM3** | | | |
|---|---|---|---|---|---|---|---|---|
| i | Dt | Dx | Dy | Dz | Dt | Dx | Dy | Dz |
| | | | | | | | | |
| 1 | 24.02219 | X1=<br>14.5761 | Y1=<br>-15.42046 | Z1=<br>-11.26109 | 23.458 | X1=<br>14.90109 | Y1= -<br>15.2501 | Z1=<br>- 9.78108 |
| 2 | 22.54937 | X2=<br>- 6.31283 | Y2=<br>-18.92332 | Z2=<br>-10.51334 | 21.73396 | X2=<br>- 6.27949 | Y2=<br>-18.8788 | Z2=<br>- 8.74779 |
| 3 | 22.38913 | X3=<br>-18.64552 | Y3=<br>-3.63554 | Z3=<br>-11.84906 | 21.54498 | X3=<br>-18.69828 | Y3=<br>- 3.62846 | Z3=<br>-10.06949 |
| 4 | 22.38099 | X4=<br>-11.56362 | Y4=<br>14.46055 | Z4=<br>-12.57315 | 21.53041 | X4=<br>-11.69506 | Y4=<br>14.49542 | Z4=<br>-10.80125 |
| 5 | 22.44077 | X5=<br>7.55462 | Y5=<br>17.30774 | Z5=<br>-12.12264 | 21.57784 | X5=<br>7.39696 | Y5=<br>17.40837 | Z5=<br>-10.38445 |
| 6 | 22.58646 | X6=<br>18.76678 | Y6=<br>2.56837 | Z6=<br>-12.30284 | 21.63747 | X6=<br>18.5810 | Y6=<br>2.74461 | Z6=<br>-10.74216 |
| Sum /n | 136.36891 / 6 | 4.37553 | -3.64266 | -70.62212 / 6 | 131.48266 / 6 | | | - 60.52622 / 6 |
| mean | 22.72815 | | | -11.770353 | 21.913777 | | | - 10.0877 |

Computed data of the individual dipole momentum of FF dipeptides obtained using PM3 RHF and Amber (after PM3) methods are presented in Table 1 (L-FF) and Table 2 (D-FF).

Schematic representation of the spatial arrangement of FF individual dipole moments ***D****ᵢ* for two coils of the PNT $\alpha$-helix (corresponding to the period of the FF structures along the main axis c) are shown in Fig. 1 for L-FF and in Fig. 2 for D-FF chiral conformations.

From our previous studies [19, 20] it is known that dipeptides L-FF form a helix structure with a right screw (D), while D-FF dipeptides create a helix with a left screw (L). These two conformations of the different FF PNT chirality is shown on these Fig. 1 and Fig. 2 with schematically selected and highlighted individual dipole moments $\boldsymbol{D_i}$ for each cases.

The calculations of chirality value (and corresponding sign obtained) were done in according with formulae (1). For greater clarity, here we give a more detailed record of this expression of the mixed vector-scalar product of three successive vectors $D_{t,i} = \{D_{x,i}; D_{y,i}; D_{z,i}\}$ for $i$ = 1, 2, 3 in the following form:

$$\left(\left[D_{t,1}, D_{t,2}\right], D_{t,3}\right) = \left(D_{t,1} \times D_{t,2}\right) \cdot D_{t,3} = \begin{vmatrix} D_{x,1} D_{y,1} D_{z,1} \\ D_{x,2} D_{y,2} D_{z,2} \\ D_{x,3} D_{y,3} D_{z,3} \end{vmatrix} =$$

$$= D_{x,1}\left(D_{y,2}D_{z,3} - D_{y,2}D_{z,2}\right) - D_{x,2}\left(D_{y,1}D_{z,3} - D_{y,3}D_{z,1}\right) + D_{x,3}\left(D_{y,1}D_{z,2} - D_{y,2}D_{z,1}\right) =$$

$$= \left(D_{y,1}D_{z,2} - D_{y,2}D_{z,1}\right)D_{x,3} - \left(D_{x,1}D_{z,2} - D_{x,2}D_{z,1}\right)D_{y,3} + \left(D_{x,1}D_{y,2} - D_{y,1}D_{x,2}\right)D_{z,3} =$$

$$= D_{t,1} \cdot \left(D_{t,2} \times D_{t,3}\right). \qquad (5)$$

Table 2. Dipole moments data for **D-FF PNT,** computed using QM **PM3 RHF** and MM **Amber** methods for 2-turns (coils) model structure of L-FF PNT, obtained on the experimental structural X-ray data. All values of dipole moments are given here in **Debye** units.

(Data presented are for one upper turn, containing 6 FF molecules, from 2 turns of $\alpha$-helix D-FF PNT model, stacked in one period of PNT structure along the c axis).

| # | **PM3 RHF** | | | | **Amber (BIO CHARM) after PM3** | | | |
|---|---|---|---|---|---|---|---|---|
| | Dt | Dx | Dy | Dz | Dt | Dx | Dy | Dz |
| 1 | 22.52289 | X1= -12.2278 | Y1= - 15.26662 | Z1= -11.16655 | 21.70719 | X1= -12.29934 | Y1= -15.17052 | Z1= -9.47542 |
| 2 | 22.36979 | X2 = 7.30246 | Y2= -18.01367 | Z2= -11.07199 | 21.52719 | X2= 7.21028 | Y2= - 17.99544 | Z2= - 9.35929 |
| 3 | 22.37242 | X3= 19.23444 | Y3= -2.59708 | Z3= -11.12526 | 21.52045 | X3= 19.16798 | Y3= - 2.65611 | Z3= - 9.41612 |
| 4 | 22.47472 | X4= 11.90525 | Y4= 15.90525 | Z4= -11.2899 | 21.62461 | X4= 11.91393 | Y4= 15.27363 | Z4= - 9.61239 |
| 5 | 22.62851 | X5= -6.61276 | Y5= 17.47797 | Z5= -12.76093 | 21.70319 | X5= - 6.4868 | Y5= 17.38568 | Z5= -11.25557 |
| 6 | 23.85476 | X6= -19.81989 | Y6= 4.38208 | Z6= -12.53070 | 23.27134 | X6= - 19.89297 | Y6= 4.72746 | Z6= -11.11199 |
| Sum /n | 136.2231 / 6 | -0.2183 | 1.88793 | -69.94533/6 | 131.35397 / 6 | | | - 60.23078 / 6 |
| mean | 22.70385 | | | -11.657555 | 21.892328 | | | - 10.038463 |

Calculations are carried out sequentially for each three vectors 1-3, 2-4, 3-5 and 4-6 and with n = 6 we get the final sum of n - 2 = 4 members in the total sum in formulae (4).

This calculation can also be carried out using a program in the language Python 3.7., written in the work of [24] for the appropriate calculation of the chirality index by the vectors connecting the Ca atoms in each $\alpha$-helix. In this case, as the normalization, one can take the approach and the corresponding expression for its calculations, developed and applied in the work [24]. It is also possible to normalize to the value of the square of the mean dipole moment.

However, it should be noted that the mixed vector-dot product is the volume of the prism built on the three vectors used. In this case, it is logical to propose a normalization to the cube of the average dipole moment for each case, as is point out in relation (4) above.

Ultimately, for comparison, Table 3 shows the calculation results for all species-normalizations, as well as the data without normalization.

The main conclusion to which we come - and this can be seen from all the calculations performed unambiguously and reliably show - that there is a change in the sign of chirality during the transition from the initial chirality of dipeptides to their helical structure in the nanotube.

The results obtained show that the ongoing change in the sign of chirality during the transition from the initial single dipeptides to the spiral structure of the nanotube, which is the next in complexity in the hierarchy of these structures, fully corresponds to the law of the change in chirality [5-8]. This can also be a confirmation of the adequacy of the proposed quantitative method for calculating the sign of chirality from the value of individual dipole moments of individual dipeptides forming a spiral structure of a nanotube.

## 4. CONCLUSIONS

The proposed method for calculating the index and sign of chirality using the values of the dipole moments of each individual dipeptides forming a helix structure of a peptide nanotube shows correct results corresponding to the law of the change in the sign of chirality, when the hierarchical structure of the molecular system becomes more complex.

This method makes it possible to numerically determine the sign of chirality in a helix structure based on the knowledge of the dipole moment of the initial dipeptides, forming the helical peptide nanotube structure.

The results obtained give us a new opportunity to see the physical basis for the formation of the type and sign of chirality and open up new possibilities for a quantitative study of this phenomenon. This approach can be applied to other similar structures and peptide nanotubes based on other amino acids and dipeptides.

## ACKNOWLEDGMENTS

The authors are greatly thankful to the Russian Foundation for Basic Researches (RFBR): grants №№ 19-01-00519_A and 20-51- 53014_ A.

The research was carried out with the support of the Interdisciplinary Scientific Educational School of Lomonosov Moscow State University "Fundamental and Applied space exploration" and partial financial support from the Russian Science Foundation: project No. 19-74-00082.

## REFERENCES

[1] A. L. Lehninger, Biochemistry. The Molecular Basis of Cell Structure and Function. New York: Worth Publishers, Inc. (1972).

[2] A.V. Finkelstein, O. B. Ptitsyn. Protein Physics: a course of lectures with color and stereoscopic illustrations and tasks. 3rd ed., rev. and suppl. Moscow: KDU, (2012). (In Russian).

[3] A. C. Mendes, E. T. Baran, R. L. Reis, H. S. Azevedo. Self-assembly in nature: using the principles of nature to create complex nanobiomaterials. *Wiley Interdiscip. Rev. Nanomed. Nanobiotechnol.* **5(6),** 582–612 (2013).

[4] Chirality and Biological Activity. Eds. Holmstedt B., Frank H., Testa B. New York: Liss, (1990).

[5] V. A. Tverdislov. Chirality as a primary switch of hierarchical levels in molecular biological systems. *Biophysics* **58** (1), 128–132 (2013).

[6] E. V. Malyshko, V. A. Tverdislov. *IOP. J. Phys. Conf. Series* **741**, 012065 (2016).

[7] V. A. Tverdislov, E. V. Malyshko, S. A. Il'chenko, O. A. Zhulyabina, L. V. Yakovenko. A periodic system of chiral structures in molecular biology. *Biophysics* **62** (3), 331–341 (2017).

[8] V. A. Tverdislov, E. V. Malyshko. On regularities in the spontaneous formation of structural hierarchies in chiral systems of nonliving and living matter. *Physics-Uspekhi* **62**, 354-363 (2019).

[9] S. F. Mason. Origins of biomolecular handedness. *Nature* **311**, 19–23 (1984).

[10] S. R. Blanke. Expanding Functionality within the Looking-Glass Universe. *Science* **325**, 1505–1506 (2009).

[11] V. S. Bystrov, P. S. Zelenovskiy, A. S. Nuraeva, S. Kopyl, O. A. Zhulyabina, V. A. Tverdislov. Chiral peculiar properties of self-organization of diphenylalanine peptide nanotubes: modeling of structure and properties. *Mathematical Biology and Bioinformatics* **14** (1), 94-124 (2019).

[12] M. R. Ghadiri, Juan R. Granja, Ronald A. Milligan, Duncan E. McRee, Nina Khazanovich. Self assembling organic nanotubes based on cyclic peptide architecture. *Nature* **366**, 324–327 (1993).

[13] C. H. Görbitz. Nanotube formation by hydrophobic dipeptides. *Chem. Eur. J.* **7**, 5153–5159 (2001).

[14] S. Scanlon, A. Aggeli. Self-assembling peptide nanotubes. *Nano Today* **3**, 22–30 (2008).

[15] V. S. Bystrov, I. Bdikin, A. Heredia, R. C. Pullar, E. Mishina, A. Sigov, A. L. Kholkin. Piezoelectricity and Ferroelectricity in biomaterials from proteins to self-assembled peptide nanotubes. In: G. Ciofani and A. Menciassi, eds. Piezoelectric nanomaterials for biomedical applications., Berlin Heidelberg, Springer-Verlag. 187-212 (2012).

[16] V. S. Bystrov. Computer Simulation Nanostructures: Bioferroelectric Peptide Nanotubes. Bioferroelectricity: Peptide Nanotubes. Saarbruecken: LAP Lambert Academic Publishing. OmniScriptum GmbH & Co. KG. (2016).

[17] V. S. Bystrov, E. Paramonova, I. Bdikin, S. Kopyl, A. Heredia, R.Pullar, A.Kholkin. BioFerroelectricity: Diphenylalanine Peptide Nanotubes Computational Modeling and Ferroelectric Properties at the Nanoscale. *Ferroelectrics* **440 (01)**, 3 – 24 (2012).

[18] V. S. Bystrov, S. A. Kopyl, P. Zelenovskiy, O. A. Zhulyabina, V. A. Tverdislov, F. Salehli, N. E. Ghermani, V. Ya. Shur & A. L. Kholkin. Investigation of physical properties of diphenylalanine peptide nanotubes having different chiralities and embedded water molecules. *Ferroelectrics* **525**, 168–177 (2018).

[19] V. S. Bystrov, P. S. Zelenovskiy, A. S. Nuraeva, S. Kopyl, O. A. Zhulyabina, V. A. Tverdislov. Molecular modeling and computational study of the chiral-dependent structures and properties of the self-assembling diphenylalanine peptide nanotubes. *J. Mol. Mod.* **25**, 199 (2019).

[20] P. S. Zelenovskiy, A. S. Nuraeva, S. Kopyl, S. G. Arkhipov, S. G. Vasilev, V. S. Bystrov, D. A. Gruzdev, M.Waliczek, V.Svitlyk, V. Ya. Shur, L. Mafra, and A.

L. Kholkin. Chirality-dependent growth of self-assembled diphenylalanine microtubes. *Cryst. Growth Des.* **19,** 6414−6421 (2019).

[21] A. Nuraeva, et al. Evaporation-Driven Crystallization of Diphenylalanine Microtubes for Microelectronic Applications. *Cryst. Growth Des.* **16**, 1472–1479 (2016).

[22] A. E. Sidorova, E. V. Malyshko, A. R. Kotov, V. A. Tverdislov, M. N. Ustinin. Quantitative Criteria of Chirality in Hierarchical Protein Structures. *Biophysics* **64** (2), 155-166 (2019).

[23] A. E. Sidorova, N. T. Levashova, E. V. Malyshko, V. A. Tverdislov. Autowave Self-Organization in the Folding of Proteins. *Moscow University Physics Bulletin* **74**(3), 213-226 (2019).

[24] A. E. Sidorova, A. O. Lutsenko, D. K. Shpigun, E. V. Malyshko, V. A. Tverdislov. Methods for Determining the Chirality sign of the Helical and Superhelical Protein Structures. *Biophysics,* (Russian Federation) **66**, 421 (2021).

[25]. RCSB PDB. Available online: http://www.rcsb.org (accessed on 15 December 2020).

[26] V. S. Bystrov, J. Coutinho, P. Zelenovskiy, A. Nuraeva, S. Kopyl, O. Zhulyabina, V. Tverdislov. Structures and properties of the self-assembling diphenylalanine peptide nanotubes containing water molecules: modeling and data analysis. *Nanomaterials* **10** (10), 1999 (2020).

[27] V.S. Bystrov, J. Coutinho, O.A. Zhulyabina, S.A. Kopyl, P.S. Zelenovskiy, A.S. Nuraeva, V.A. Tverdislov, S.V. Filippov, A.L. Kholkin, V.Ya. Shur. Modelling and physical properties of diphenylalanine peptide nanotubes containing water molecules. *Ferroelectrics* (2021). (in press).

[28] VASP (Vienna Ab initio Simulation Package). Available online: https://www.vasp.at/ (accessed on 27 December 2020).

[29] Hypercube Inc. HyperChem, versions 7.51 and 8.0; Hypercube Inc.: Gainesville, FL, USA, 2002. Available online: http://www.hyper.com/?tabid=360 (accessed on 27 December 2020).

[30] The Cambridge Crystallographic Data Centre (CCDC). Available online: https://www.ccdc.cam.ac.uk/ (accessed on 27 December 2020).

NANOMATERIALS
SCIENCE & ENGINEERING
Vol. 3, No. 1, pp. 22-30 (2021)

RESEARCH ARTICLE

https://doi.org/10.34624/nmse.v3i1.24058

# Facile Hydrothermal Synthesis of $CoFe_2O_4/Co_3O_4$ Nanostructures for Efficient Oxygen Evolution Reaction

**Pratik V. Shinde[1], Rutuparna Samal[1], Manoj Kumar Singh[2, *], Chandra Sekhar Rout[1, *]**

[1]*Centre for Nano and Material Sciences, Jain University, Jain Global Campus, Jakkasandra, Ramanagaram, Bangalore-562112, Karnataka, India*
[2]*Department of Physics under School of Engineering and Technology (SOET), Central University of Haryana (CUH), Mahendergarh- 123031, Haryana, India*
**Corresponding authors, e-mail addresses: r.chandrasekhar@jainuniversity.ac.in; manojksingh@cuh.ac.in*

Received 1 March 2021; accepted 25 March 2021; published online 30 March 2021

## ABSTRACT

Co/Fe-based spinel oxide materials play an important role in the development of non-precious-metal-based electrocatalysts toward water splitting. Herein, we have synthesized the $CoFe_2O_4/Co_3O_4$ nanostructures via the facile hydrothermal method. $CoFe_2O_4/Co_3O_4$ nanostructures exhibited a low overpotential of 311 mV @10 mA/cm$^2$, a small Tafel slope of 87 mV/dec, as well as remarkable long-term stability towards OER. The performance of $CoFe_2O_4/Co_3O_4$ nanostructures is considerably higher than that of bare $CoFe_2O_4$ and $Co_3O_4$ materials. The outstanding performance is mainly attributed to the synergistic effect and increased active sites for OER reactions. This study can pave a pathway for engineering non-noble metal-based efficient, cost-effective, and durable electrocatalysts for OER.

## 1. INTRODUCTION

With the rapid depletion of fossil fuels and the associated environmental issues, the development of alternative clean energy sources is crucial. Numerous innovative, as well as trending concepts regarding energy storage/conversion, have recently been incorporated for achieving sustainable and environmental friendly systems such as water electrolysis, supercapacitors, fuel cells, and metal-air batteries. Electrochemical water splitting is considered as a promising approach among the above to obtain clean hydrogen fuels from renewable energy sources. The electrochemical splitting of water involves two crucial reactions, the cathode part involves hydrogen evolution reaction (HER) and the anode part ensues oxygen evolution reaction (OER) [1]. pH-dependent OER reaction is important owing to its impact on water splitting electrochemistry wherein molecular oxygen is produced at the anode via several proton/electron transition reactions [2]. As OER involves a four-electron transfer process with the breaking of O-H bonds and the formation of O-O bonds, the reaction needs a high overpotential [3]. In-depth investigation for a suitable oxygen evolution electrocatalyst, substantial efforts have been devoted in recent times but meeting the practical application is still underway. Currently, Ru and Ir-based materials are the most efficient electrocatalysts for OER however, their cost and scarcity limit their large-scale practical applications [4, 5]. Both of the typical OER catalysts $RuO_2$ and $IrO_2$ oxidize to $RuO_4$ and $IrO_3$ respectively at the application of high anodic potential in acidic and alkaline electrolytes. Improvement in the electrocatalysts in terms of flexibility, production of high purity gases, low cost, high efficiency, and durability is highly essential. Hence, extensive research efforts have been dedicated to the development of efficient electrocatalysts for the OER reactions. Earth-abundant materials have been widely used as electrocatalysts which demonstrated significant OER performance [6-8].

Considering chemical stability requirements towards the practical application, transition metal oxides can be looked upon as promising candidates. As compared to the single metal oxide, bimetal spinel oxides such as $CoFe_2O_4$, $NiFe_2O_4$, $MnFe_2O_4$, etc., show significant electrocatalytic performance for oxygen evolution reaction [9-11]. Generally, spinel oxide structure is represented as $AB_2O_4$, here A and B are metals in tetrahedral and octahedral sites, respectively [12]. The properties such as high abundance, low toxicity, rich redox chemistry, and superior stability make these class materials promising for energy applications [13, 14]. Precisely, cobalt ferrite ($CoFe_2O_4$) has gained particular interest in catalysis because of its earth abundance, environmental friendliness, high electrical conductivity, and sound durability [15, 16].

Herein, a simple hydrothermal method was adopted to prepare $CoFe_2O_4/Co_3O_4$ nanostructure. $CoFe_2O_4/Co_3O_4$ nanostructure exhibits a low overpotential of 311 mV at 10 mA/cm$^2$ for OER reaction. The as-prepared catalyst exhibited appreciable activity, a lower Tafel slope, and good stability in OER electrocatalysis. The present study offers a facile and efficient route to synthesize spinel metal oxides as a catalyst for high-performance OER reactions.

## 2. EXPERIMENTAL

### 2.1. Chemicals

The purities of all the reagents used are of analytical grade and used without further purification. Cobalt Nitrate [$Co(NO_3)_2.6H_2O$] was purchased from Sisco Research Laboratories Pvt. Ltd., iron nitrate [$Fe(NO_3)_3 \cdot 9H_2O$], and urea [$NH_2CONH_2$] were procured from SD-Fine Chem Limited.

### 2.2. Synthesis

In a typical procedure for the preparation of $CoFe_2O_4/Co_3O_4$ material, cobalt nitrate (1.2 g), iron nitrate (1.2 g), and urea (0.7 g) were dissolved independently in 20 mL distilled (DI) water. After 30 min stirring, solutions were mixed together and stirred for another 1 h at room temperature. Subsequently, the homogenous mixture was transferred into a 100 mL Teflon-lined stainless-steel autoclave and maintained at 120 ºC for 16 h. After complete processing in a hot-air oven, the autoclave was cooled down to room temperature naturally. The obtained precipitate was washed several times with DI water and ethanol to remove any possible impurities and further dried in a vacuum oven at 90 ºC for 6 h. Finally, as prepared $CoFe_2O_4/Co_3O_4$ material was calcined at 750 °C for 2 h in a muffle furnace. Additionally, $CoFe_2O_4$ and $Co_3O_4$ materials were also synthesized by following a similar procedure wherein, 0.8 g cobalt nitrate was used to prepare $CoFe_2O_4$ material while for $Co_3O_4$ preparation, iron nitrate source was eliminated.

### 2.3. Characterizations

The crystal structure of the synthesized powder was identified by a Rigaku Ultima IV X-ray diffractometer having Ni-filter for Cu Kα radiation (wavelength, λ = 1.541 Å) at a scanning rate of 2°/min. Field emission scanning electron microscopy (FESEM) was performed with JEOL JSM-7100F, JEOL Ltd., Singapore to observe morphologies of the prepared materials. The energy dispersive spectrometer (EDAX) is equipped with a FESEM instrument used for the elemental analysis of the material. For understanding the functionalization of materials Fourier-transform infrared spectroscopy (FTIR) was recorded on the Perkin Elmer spectrophotometer using KBr pellets. The electrochemical study was performed on the CorrTest-CS350, China workstation.

### 2.4. Characterizations

Electrochemical measurements were performed within a three-electrode electrochemical cell with 0.5 M KOH electrolyte. Prepared electrocatalyst (2 mg) and Nafion solution (10 µL) were dispersed in isopropanol (200 µL) with the assistance of vigorous sonication (30 min) to form a homogeneous ink. The ink was then loaded onto a nickel foam in the area of 0.5 x 0.5 cm$^2$. The

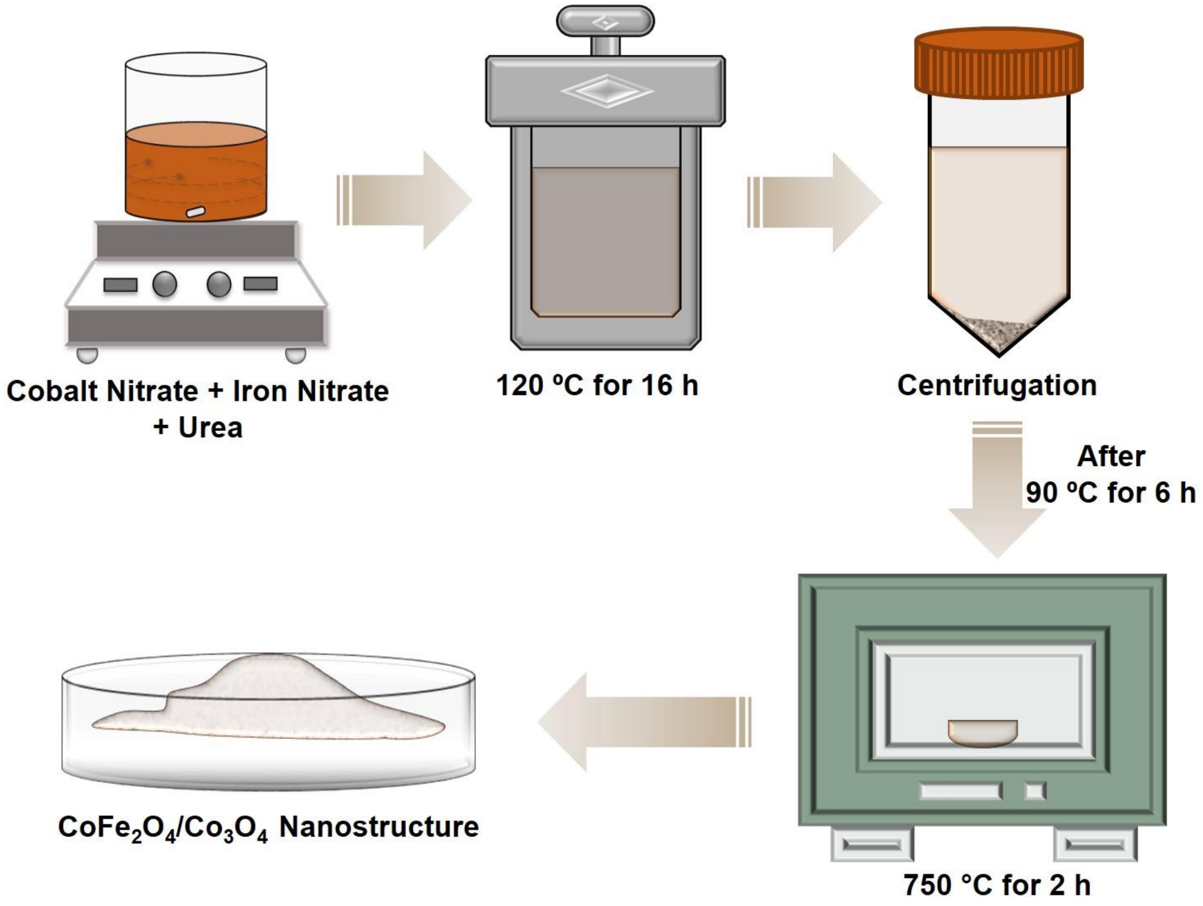

Figure 1. Schematic illustration of the synthesis of $CoFe_2O_4/Co_3O_4$ nanostructure.

Ag/AgCl electrode worked as the reference electrode, and a platinum wire was employed an auxiliary electrode.

All the potentials reported in the present work has been converted to the reversible hydrogen electrode (RHE) using the following equation [3],

$$E_{(RHE)} = E_{(Ag/AgCl)} + 0.059\ \text{pH} + 0.197\ \text{V} \qquad (1)$$

To evaluate the OER activity of as-prepared samples, linear sweep voltammetry (LSV) curves were recorded at a scan rate of 5 mV/s.

Tafel plots of overpotential vs. log (j) are fitted to the Tafel equation [3],

$$\eta = b \log |j| + a \qquad (2)$$

where $\eta$ is overpotential, $j$ is the current density, and $b$ is the Tafel slope.

Electrochemical impedance spectroscopy (EIS) was measured at an overpotential of 311 mV vs. RHE in frequency ranges from 1 MHz to 0.01 Hz. Chronoamperometry was measured under a constant potential of 1.54 V vs. RHE over 10000 s.

## 3. RESULTS AND DISCUSSION

The schematic representation for the synthesis of $CoFe_2O_4/Co_3O_4$ nanostructures is illustrated in **Figure 1**. The $CoFe_2O_4/Co_3O_4$ nanostructures were prepared by a facile hydrothermal synthesis method using metal nitrate precursors followed by calcination in air.

### 3.1. Characterization

XRD measurement was employed to analyze the crystallographic phases of the synthesized materials. The obtained XRD patterns of the prepared catalyst are shown in **Figure 2**. The planes (111), (220), (311), (222), (400), (422), (511), and (440) correspond to the $CoFe_2O_4$ spinel structure. Whereas, the plane (111), (220), (311),

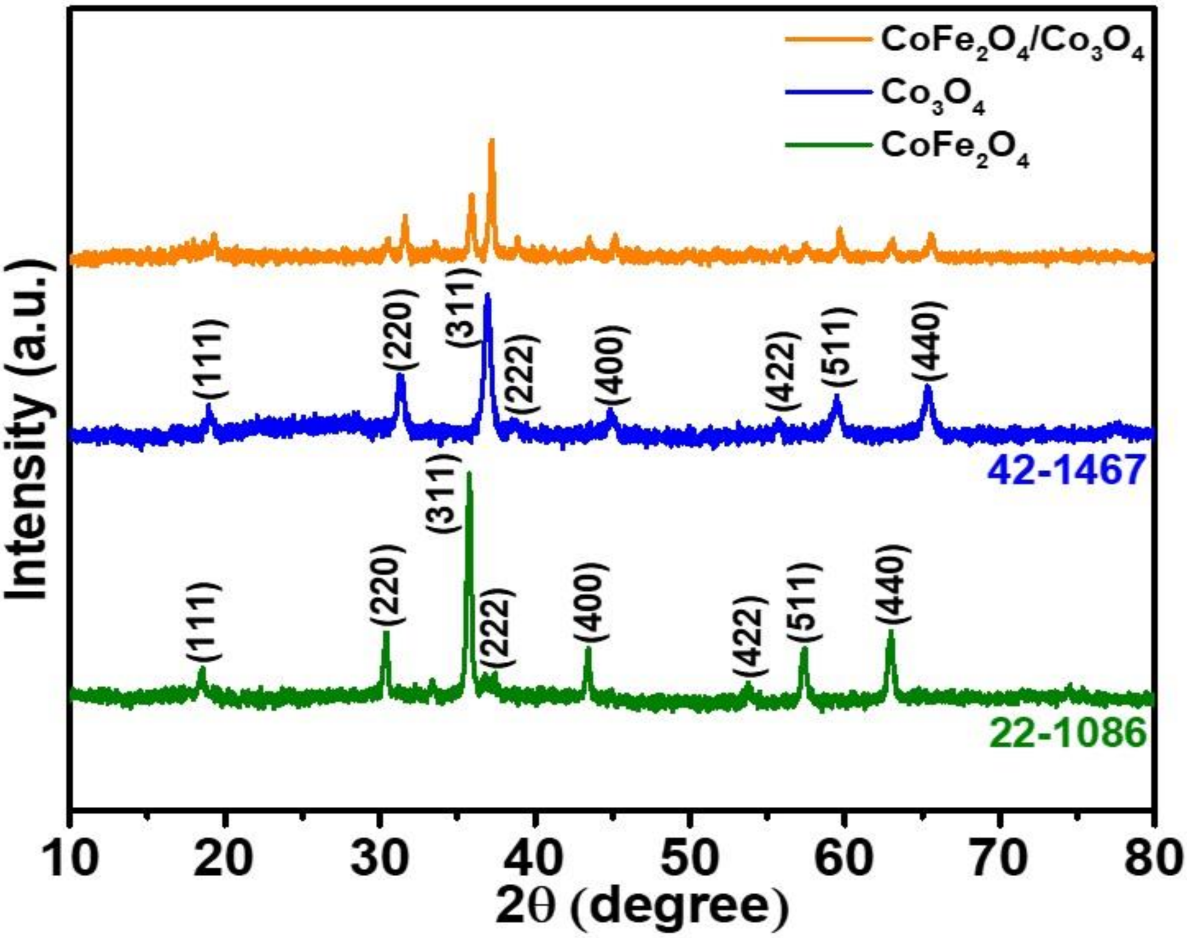

Figure 2. XRD patterns of the CoFe$_2$O$_4$, Co$_3$O$_4$ and CoFe$_2$O$_4$/Co$_3$O$_4$ nanostructures.

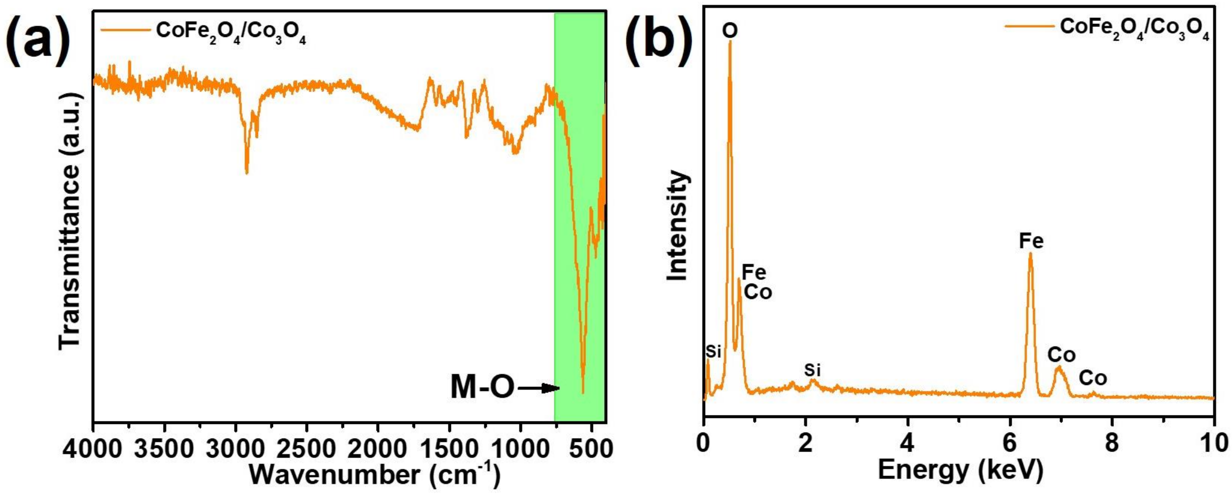

Figure 3. (a) FT-IR spectrum and (b) EDAX of the CoFe$_2$O$_4$/Co$_3$O$_4$ nanostructure.

(222), (400), (422), (511), and (440) can be ascribed to the Co$_3$O$_4$. All of the diffraction peaks coincided with the standard values of cubic spinel CoFe$_2$O$_4$ (JCPDS no. 22-1086) and cubic Co$_3$O$_4$ (JCPDS no. 42-1467). Other than standard peaks, no secondary characteristic peaks of any type of impurities or other phases are detected. Clearly, we can perceive that CoFe$_2$O$_4$/Co$_3$O$_4$

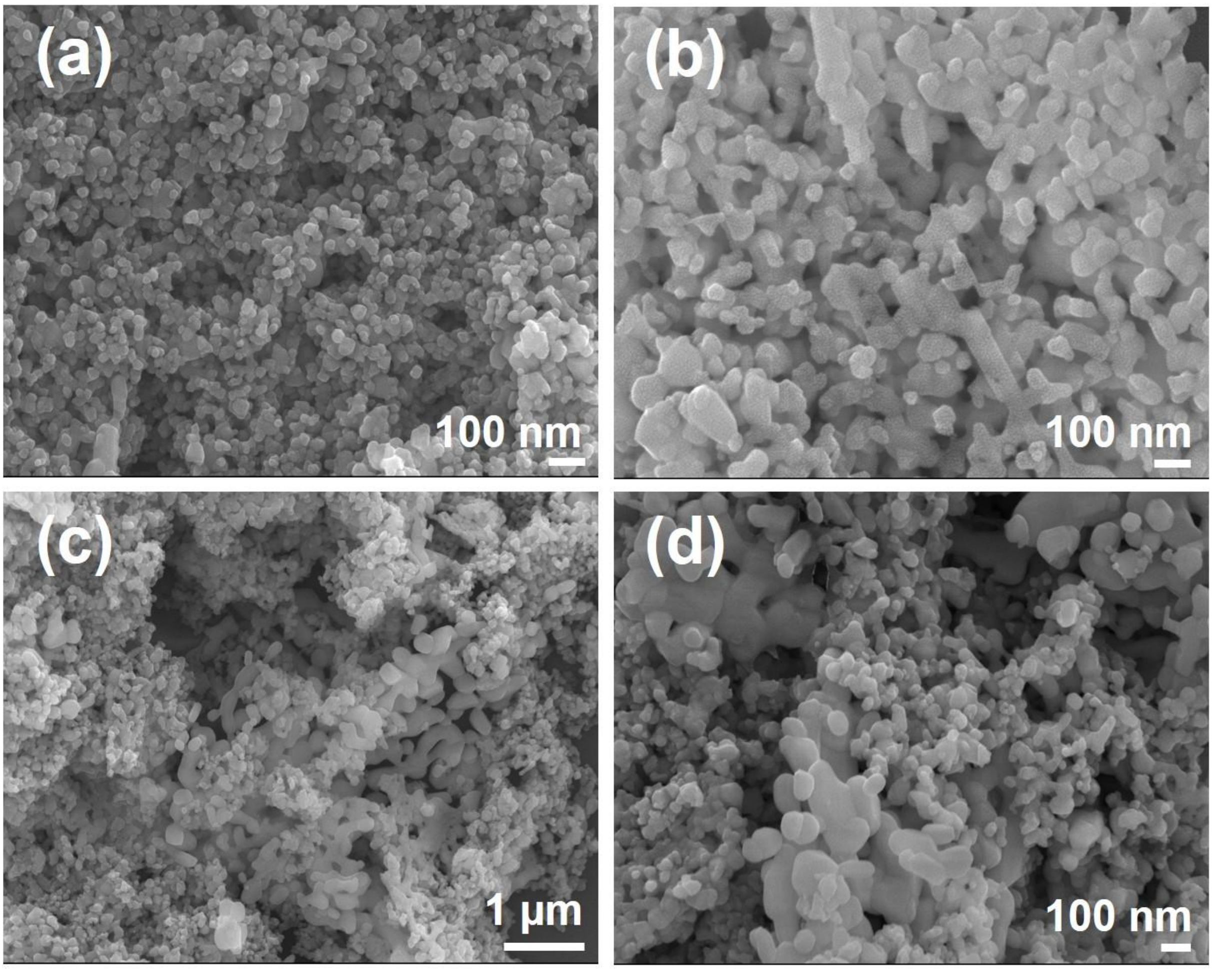

Figure 4. High resolution FE-SEM image of the (a) $CoFe_2O_4$, (b) $Co_3O_4$, (c-d) $CoFe_2O_4/Co_3O_4$ nanostructure.

nanostructures reveal the co-occurrence of $CoFe_2O_4$ and $Co_3O_4$.

FT-IR spectroscopy is a useful tool to identify the functional group of the molecule. FT-IR spectrum of the $CoFe_2O_4/Co_3O_4$ nanostructure was recorded in the range of 450-4000 $cm^{-1}$ (**Figure 3a**). The appearance of a peak in the range of 400-600 $cm^{-1}$ is attributed to the metal-oxygen (M-O) stretching vibrations [17]. A sharp peak at around 1600 $cm^{-1}$ and broadband near 3400 $cm^{-1}$ is related to the deformation vibrations of adsorbed $H_2O$ molecules and stretching vibrations of O-H on the catalyst surface, respectively [17-18]. Typical EDAX analysis of the resulted $CoFe_2O_4/Co_3O_4$ nanostructures is shown in **Figure 3b**, which indicated the existence of Co, Fe, and O elements. The morphologies and structural features of the synthesized $CoFe_2O_4$, $Co_3O_4$, and $CoFe_2O_4/Co_3O_4$ nanostructures were observed directly from the FE-SEM images. **Figure 4a-d**, shows that the as-prepared $CoFe_2O_4/Co_3O_4$ sample inherits the multi-shape nanostructure morphology of the original $CoFe_2O_4$ and $Co_3O_4$. EDAX mapping was performed to confirm the elemental composition of $CoFe_2O_4/Co_3O_4$ nanostructures. EDAX mapping reveals the uniform distribution of Co, Fe, and O as shown in **Figure 5a-d**. The atomic percentages of Co, Fe, and O elements were 27 %, 15 %, and 58 %, respectively.

### 3.2. Oxygen Evolution Reaction

The electrocatalytic behavior of as-prepared catalysts was then investigated by a three-electrode configuration in 0.5 M KOH electrolyte. LSV curves for oxygen evolution reaction are shown in **Figure 6a**. The required overpotential of $CoFe_2O_4/Co_3O_4$ nanostructure to achieve the

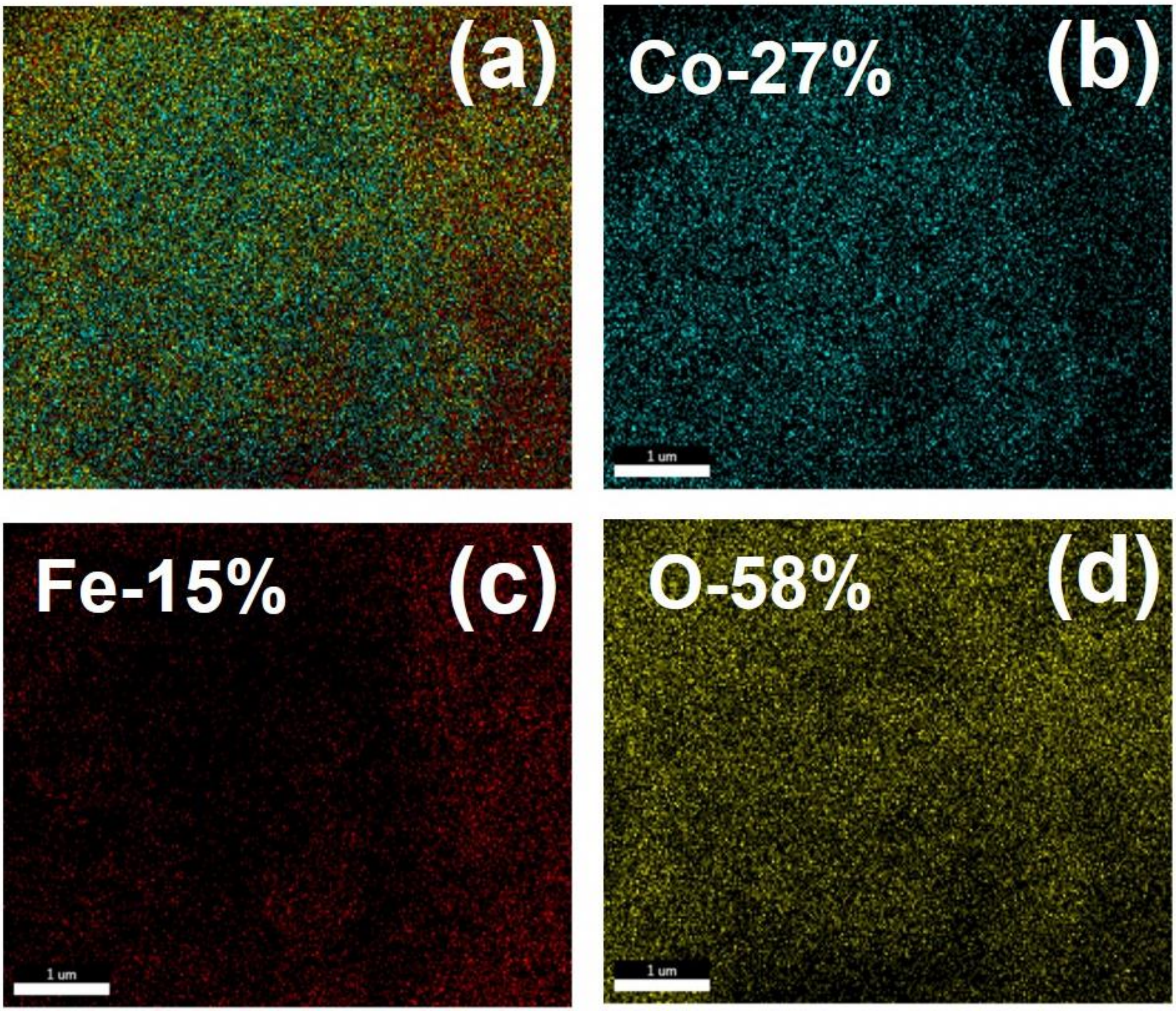

Figure 5. (a) Elemental mapping of the $CoFe_2O_4/Co_3O_4$ , (b) Co, (c) Fe, (d) O.

active current density of 10 mA/cm$^2$ is only 311 mV, which is much lower than those of $CoFe_2O_4$ (351 mV), and $Co_3O_4$ (391 mV). The findings reveal that $CoFe_2O_4/Co_3O_4$ nanostructure demonstrated a remarkable activity towards OER reaction. A comparative Tafel plot was constructed by using the LSV graphs, to gain more insight into the kinetics of OER performance. For an electrocatalytically active catalyst, the smaller the value of the Tafel slope, the faster is the rate of reaction. **Figure 6b** illustrates the Tafel slope value of 141 mV/dec and 158 mV/dec derived for pure $CoFe_2O_4$ and $Co_3O_4$, respectively. However, a relatively small Tafel slope value of 87 mV/dec is observed for $CoFe_2O_4/Co_3O_4$ nanostructure. Impressively, the estimated Tafel slope of $CoFe_2O_4/Co_3O_4$ nanostructure (87 mV/dec) is far better than those of the well-established OER catalysts such as $RuO_2$ (119 mV/dec). EIS was used to examine the charge transfer kinetics of the working electrode. **Figure 6c** shows the Nyquist plots for pure $CoFe_2O_4$, pure $Co_3O_4$, and $CoFe_2O_4/Co_3O_4$ nanostructure, which were fitted to a simplified Randles circuit. A semicircle was observed in the high-frequency region and its diameter attributes to the charge transfer resistance ($R_{ct}$). A much lower solution resistance ($R_s$) and charge transfer resistance ($R_{ct}$) were observed over the $CoFe_2O_4/Co_3O_4$ nanostructure than that for pure $CoFe_2O_4$ and $Co_3O_4$. A slow charge transfer resistance improved the electrical conductivity and hence EIS revealed that $CoFe_2O_4/Co_3O_4$ nanostructure exhibits high electrochemical performance for OER. Long-term stability is another key parameter to evaluate excellent OER electrocatalysts. To evaluate the durability of the $CoFe_2O_4/Co_3O_4$ nanostructure in the process of OER, chronoamperometry tests

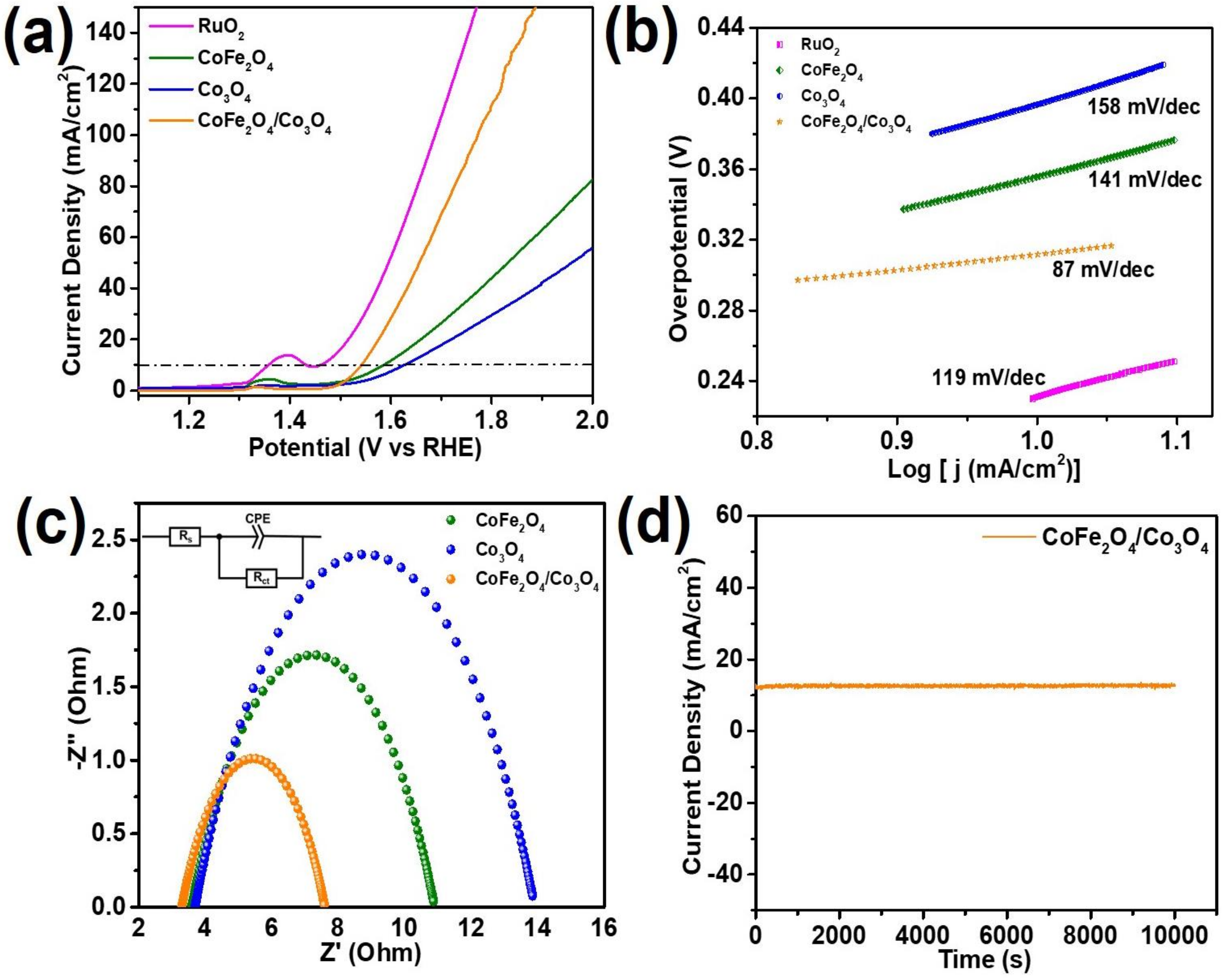

Figure 6. Electrocatalytic performance: (a) LSV curves, (b) Corresponding Tafel slopes, (c) Nyquist's plots, Inset: Randle's circuit, (d) Chronoamperometry plot at a potential of 1.54 V.

Table 1. OER performance of synthesized $CoFe_2O_4/Co_3O_4$ nanostructure catalyst and $RuO_2$.

| Sr. No. | Electrocatalyst | Overpotential (mV) @10 mA/cm$^2$ | Tafel Slope (mV/dec) |
|---|---|---|---|
| 1 | $RuO_2$ | 236 | 119 |
| 2 | $CoFe_2O_4$ | 351 | 141 |
| 3 | $Co_3O_4$ | 391 | 158 |
| **4** | **$CoFe_2O_4/Co_3O_4$** | **311** | **87** |

were performed at 1.54 V vs. RHE as shown in **Figure 6d**. Stable performance was observed over 10000 s without a decline in current density. The overall OER performance of synthesized $CoFe_2O_4/Co_3O_4$ nanostructure catalyst and reported $RuO_2$ is compared in **Table 1**. The high OER performance of $CoFe_2O_4/Co_3O_4$ nanostructure is attributed to the synergistic effect of $CoFe_2O_4$ and $Co_3O_4$, which accelerated the charge transfer between active sites and intermediates.

## 4. CONCLUSIONS

In conclusion, we have demonstrated the application of $CoFe_2O_4/Co_3O_4$ nanostructure for OER performance. Owing to the enhanced conductivity and quick reaction dynamics, the $CoFe_2O_4/Co_3O_4$ nanostructure electrocatalyst yielded high catalytic activity. The catalyst exhibited a low overpotential of 311 mV @10 mA/cm$^2$, a small Tafel slope of 87 mV/dec, and excellent long-term durability. The OER activities of transition metal oxides are dependent on the oxidation state, the number of 3d electrons of the metal atom as well as the binding energies of the oxygen atoms. Especially, the multivalent oxidation states $M^{+2/+3/+4}$ of $CoFe_2O_4/Co_3O_4$ were responsible for the creation of additional active sites in the hybrid system proving it to be an excellent candidate for oxygen evolution reactions. The increased number of active sites and synergistic effect enhanced the OER performance of the $CoFe_2O_4/Co_3O_4$ nanostructure. With the merit of cost-effective, earth-abundant, and efficient OER performance, $CoFe_2O_4/Co_3O_4$ nanostructure could be a promising non-noble electrocatalyst for water splitting.

## ACKNOWLEDGMENTS

The authors would like to acknowledge financial support from SERB Early Career Research project (Grant No. ECR/2017/001850), Department of Science and Technology (DST/NM/NT/2019/205(G); DST/TDT/SHRI-34/2018), Karnataka Science and Technology Promotion Society (KSTePS/VGST-RGS-F/2018-19/GRD NO. 829/315), start-up grant, Jain University (11 (39)/17/013/2017SG), Nanomission (SR/NM/NS-20/2014) for the characterization facilities.

## REFERENCES

[1] M. I. Jamesh, Y. Kuang, X. Sun, Constructing Earth-abundant 3D Nanoarrays for Efficient Overall Water Splitting–A Review, *ChemCatChem* **11**, 1550-1575, (2019).

[2] J. Song, C. Wei, Z.F. Huang, C. Liu, L. Zeng, X. Wang, Z.J. Xu, A review on fundamentals for designing oxygen evolution electrocatalysts, *Chemical Society Reviews* **49**, 2196-2214, (2020).

[3] P. Shinde, C.S. Rout, D. Late, P.K. Tyagi, M.K. Singh, Optimized performance of nickel in crystal-layered arrangement of $NiFe_2O_4$/rGO hybrid for high-performance oxygen evolution reaction, *International Journal of Hydrogen Energy*, **46**, 2617-2629, (2021).

[4] Y. Ma, H. Zhang, J. Xia, Z. Pan, X. Wang, G. Zhu, B. Zheng, G. Liu, L. Lang, Reduced $CoFe_2O_4$/graphene composite with rich oxygen vacancies as a high efficient electrocatalyst for oxygen evolution reaction, *International Journal of Hydrogen Energy*, **45**, 11052-11061, (2020).

[5] Q. Shi, C. Zhu, D. Du, Y. Lin, Robust noble metal-based electrocatalysts for oxygen evolution reaction, *Chemical Society Reviews*, **48**, 3181-3192, (2019).

[6] L. Li, Y. Zhang, J. Li, W. Huo, B. Li, J. Bai, Y. Cheng, H. Tang, X. Li, Facile synthesis of yolk–shell structured $ZnFe_2O_4$ microspheres for enhanced electrocatalytic oxygen evolution reaction, *Inorganic Chemistry Frontiers*, **6**, 511-520, (2019).

[7] Y. Liu, Z. Niu, Y. Lu, L. Zhang, K. Yan, Facile synthesis of $CuFe_2O_4$ crystals efficient for water oxidation and $H_2O_2$ reduction, *Journal of Alloys and Compounds*, **735**, 654-659, (2018).

[8] H.Y. Wang, Y.Y. Hsu, R. Chen, T.S. Chan, H.M. Chen, B. Liu, $Ni^{3+}$-induced formation of active NiOOH on the spinel Ni–Co oxide surface for efficient oxygen evolution reaction, *Advanced Energy Materials*, **5**, 1500091, (2015).

[9] M. Sun, D. Lin, S. Wang, T. Zhang, D. Wang, J. Li, Facile synthesis of $CoFe_2O_4$-$CoFe_x$/C nanofibers electrocatalyst for the oxygen evolution reaction, *Journal of The Electrochemical Society*, **166**, H412, (2019).

[10] X. Chen, X. Zhang, L. Zhuang, W. Zhang, N. Zhang, H. Liu, T. Zhan, X. Zhang, X. She, D. Yang, Multiple Vacancies on (111) Facets of Single-Crystal $NiFe_2O_4$ Spinel Boost Electrocatalytic Oxygen Evolution Reaction, *Chemistry–An Asian Journal*, **15**, 3995-3999, (2020).

[11] Z. Zhang, D. Zhou, S. Zou, X. Bao, X. He, One-pot synthesis of $MnFe_2O_4$/C by microwave sintering as an efficient bifunctional electrocatalyst for oxygen reduction and oxygen evolution reactions, *Journal of Alloys and Compounds*, **786**, 565-569, (2019).

[12] J.A. Rajesh, B.K. Min, J.H. Kim, H. Kim, K.S. Ahn, Cubic spinel $AB_2O_4$ type porous $ZnCo_2O_4$ microspheres: facile hydrothermal synthesis and their electrochemical performances in pseudocapacitor, *Journal of The Electrochemical Society*, **163**, A2418, (2016).

[13] V.D. Silva, L.S. Ferreira, T.A. Simões, E.S. Medeiros, D.A. Macedo, 1D hollow $MFe_2O_4$ (M= Cu, Co, Ni) fibers by Solution Blow Spinning for oxygen evolution reaction, *Journal of colloid and Interface Science*, **540**, 59-65, (2019).

[14] Y. Chen, Z. Shi, S. Li, J. Feng, B. Pang, L. Yu, W. Zhang, L. Dong, N, S-codoped graphene supports for Ag-$MnFe_2O_4$ nanoparticles with improved

performance for oxygen reduction and oxygen evolution reactions, *Journal of Electroanalytical Chemistry*, **860**, 113930, (2020).

[15] T. Li, Y. Lv, J. Su, Y. Wang, Q. Yang, Y. Zhang, J. Zhou, L. Xu, D. Sun, Y. Tang, Anchoring $CoFe_2O_4$ nanoparticles on N-doped carbon nanofibers for high-performance oxygen evolution reaction, *Advanced Science*, **4**, 1700226, (2017).

[16] D. Xu, B. Liu, G. Liu, K. Su, C. Yang, H. Tong, D. Qian, J. Li, N-doped bamboo-like CNTs combined with CoFe–$CoFe_2O_4$ as a highly efficient electrocatalyst towards oxygen evolution, *International Journal of Hydrogen Energy*, **45**, 6629-6635, (2020).

[17] Z. Rahimi, H. Sarafraz, G. Alahyarizadeh, A.S. Shirani, Hydrothermal synthesis of magnetic $CoFe_2O_4$ nanoparticles and $CoFe_2O_4$/MWCNTs nanocomposites for U and Pb removal from aqueous solutions, *Journal of Radioanalytical and Nuclear Chemistry*, **317**, 431-442, (2018).

[18] V.P. Senthil, J. Gajendiran, S.G. Raj, T. Shanmugavel, G.R. Kumar, C.P. Reddy, Study of structural and magnetic properties of cobalt ferrite ($CoFe_2O_4$) nanostructures, *Chemical Physics Letters*, **695**, 19-23, (2018).

**Nanomaterials Science & Engineering (NMS&E), Vol.3, No.1, 2021**

NMS&E

**Department of Mechanical Engineering**
**University of Aveiro**
**Aveiro 3810-193**
**Portugal**

**https://proa.ua.pt/index.php/nmse/**

**ISSN: 2184-7002**

university of aveiro tema centre for mechanical technology and automation